Magnetic Fields and Rotations of Protostars

Masahiro N. Machida[1] and Shu-ichiro Inutsuka[1], and Tomoaki Matsumoto[2]

ABSTRACT

The evolution of the magnetic field and angular momentum in the collapsing cloud core is studied using three-dimensional resistive MHD nested grid simulations. Starting with a Bonnor-Ebert isothermal cloud rotating in a uniform magnetic field, we calculate the cloud evolution from the molecular cloud core ($n_c \simeq 10^4\,\mathrm{cm}^{-3}$, $r = 4.6 \times 10^5\,\mathrm{AU}$) to the stellar core ($n_c \simeq 10^{22}\,\mathrm{cm}^{-3}$, $r \sim 1 R_\odot$), where n_c and r denote the central density and radius of each object, respectively. The magnetic field strengths at the center of the clouds converge to a certain value as the clouds collapse for $n_c \lesssim 10^{12}\,\mathrm{cm}^{-3}$, when the clouds have the same angular momenta but different strengths of the magnetic fields at the initial state. For $10^{12} \lesssim n_c \lesssim 10^{16}\,\mathrm{cm}^{-3}$, Ohmic dissipation considerably removes the magnetic field from the collapsing cloud core, and the magnetic field lines, which are strongly twisted for $n_c \lesssim 10^{12}\,\mathrm{cm}^{-3}$, is de-collimated. The magnetic field lines are twisted and amplified again for $n_c \gtrsim 10^{16}\,\mathrm{cm}^{-3}$, because the magnetic field is recoupled with the warm gas for $n_c \gtrsim 10^{16}\,\mathrm{cm}^{-3}$. Finally, protostars at their formation epoch ($n_c \simeq 10^{21}\,\mathrm{cm}^{-3}$) have $\sim$0.1–1 kG of the magnetic fields, which are comparable to observations. The magnetic field strength of protostar slightly depends on the angular momentum of the host cloud. The protostar formed from the slowly rotating cloud core has a stronger magnetic field. The evolution of the angular momentum is closely related to the evolution of the magnetic field. The angular momentum in the collapsing cloud is removed by the magnetic effect (magnetic braking, outflow and jet). The formed protostars have 0.1–2 days of the rotation period at their formation epoch, which are slightly shorter than the observation. This indicates that the further removal mechanism of the angular momentum such as interaction between the protostar and disk, wind gas or jet is important in further evolution of the protostar.

Subject headings: ISM: clouds: ISM: magnetic fields—MHD—stars: formation—stars: rotation

[1]Department of Physics, Graduate School of Science, Kyoto University, Sakyo-ku, Kyoto 606-8502, Japan; machidam@scphys.kyoto-u.ac.jp, inutsuka@tap.scphys.kyoto-u.ac.jp

[2]Faculty of Humanity and Environment, Hosei University, Fujimi, Chiyoda-ku, Tokyo 102-8160, Japan; matsu@i.hosei.ac.jp

1. Introduction

The Lorentz and centrifugal forces play important roles for the star formation process. The gravity and thermal pressure are isotropic forces, while the Lorentz and centrifugal forces are anisotropic forces that are closely related to the disk formation, outflows, and jets in the collapsing cloud. Molecular clouds have $\sim 2\%$ of the rotational energy against the gravitational energy (Goodman et al. 1993; Caselli 2002). On the other hand, the clouds have the magnetic energy comparable to the gravitational energy (Crutcher 1999). By simply considering the conservation of the magnetic flux and angular velocity, it is found that the effect of the rotation and magnetic field in the cloud gradually increases as the cloud collapses. However, the magnetic field strength and angular velocity of the observed protostars indicate that both of the magnetic flux and angular momentum are not conserved in the collapsing clouds. In general, they are called as 'Magnetic flux problem' and 'angular momentum problem.' The former is the problem that the magnetic flux of the molecular cloud is much larger than that of protostar compared with equivalent mass. The latter is the problem that the specific angular momentum of the molecular cloud is much larger than that of protostar. Thus, both of the magnetic flux and angular momentum should be removed from the cloud core by some mechanisms. In the collapsing cloud, these two problems are mutually related. For example, the angular momentum is removed by the magnetic effect (i.e., the magnetic braking, outflows, and jets), while magnetic field is amplified by shearing motion caused from the cloud rotation. Thus, we cannot treat either of the magnetic field or the rotation independently for considering the magnetic flux and angular momentum problems. In addition, it is difficult to treat the evolution of the magnetic field and rotation analytically since the density ($n \sim 10^4\,\mathrm{cm}^{-3}$) and scale ($R \sim 10^4\,\mathrm{AU}$) of the molecular clouds are much different from those of protostar ($n \sim 10^{24}\,\mathrm{cm}^{-3}$, $R \sim 1\,R_\odot$). Therefore, numerical simulation is needed to study the magnetic field and rotation of protostars formed from molecular clouds.

Angular momentum is removed by the magnetic braking and outflow from the collapsing cloud as shown by Basu & Mouschovias (1994), Tomisaka (2002), and Machida et al. (2005a). Machida et al. (2005a) shows that about 70% of the total angular momentum is removed from the collapsing cloud core for the isothermal phase ($n \lesssim 10^{11}\,\mathrm{cm}^{-3}$). Tomisaka (2002) shows that $\sim$99% of the total angular momentum is transferred by the outflow for the adiabatic phase ($10^{11}\,\mathrm{cm}^{-3} \lesssim n \lesssim 10^{16}\,\mathrm{cm}^{-3}$). Thus, previous studies show that angular momentum is effectively transferred by the magnetic effect. In contrast, there are a few studies about the evolution and removal process of the magnetic flux in the collapsing cloud core especially for high density ($n \gtrsim 10^{12}\,\mathrm{cm}^{-3}$). Nakano et al. (2002) analytically investigate the dissipation process of the magnetic field in the collapsing cloud core, and show that the magnetic flux is expected to be removed from the cloud core largely during

$10^{12}\,\mathrm{cm}^{-3} \lesssim n \lesssim 10^{16}\,\mathrm{cm}^{-3}$.

To investigate the evolution of the magnetic field and rotation (or the magnetic flux and angular momentum problems), we need to calculate the cloud evolution from molecular cloud core ($n \simeq 10^4\,\mathrm{cm}^{-3}$) to protostar formation ($n \sim 10^{24}\,\mathrm{cm}^{-3}$), taking account of the magnetic field and rotation. The evolution of magnetized cloud until central density reaches $n \simeq 10^{15}\,\mathrm{cm}^{-3}$ is investigated by Hosking & Whitworth (2004), Ziegler (2005), Matsumoto & Tomisaka (2004), and Machida et al. (2004, 2005a,b). Tomisaka (2002) and Banerjee & Pudritz (2006) calculate the cloud evolution until the protostar is formed ($n \sim 10^{21}\,\mathrm{cm}^{-3}$), and show that the magnetic field has important roles for the star-formation process. However, they adopt ideal MHD approximation, which is valid in low-density gas region ($n \lesssim 10^{12}\,\mathrm{cm}^{-3}$), however, not valid in high-density gas region ($n \gtrsim 10^{12}\,\mathrm{cm}^{-3}$). Therefore, Tomisaka (2002) and Banerjee & Pudritz (2006) overestimate the magnetic flux in the collapsing cloud especially in high-density gas region, because significant magnetic flux loss occurs during $10^{12}\,\mathrm{cm}^{-3} \lesssim n \lesssim 10^{15}\,\mathrm{cm}^{-3}$ by Ohmic dissipation (Nakano et al. 2002).

Following to Machida et al. (2006b), we report results of three-dimensional non-ideal MHD nested grid simulations in detail. In this paper, we calculate the cloud evolution from cloud core ($n_c \simeq 10^4\,\mathrm{cm}^{-3}$, $r_c = 4.6 \times 10^5\,\mathrm{AU}$) to protostar formation ($n_c \simeq 10^{22}\,\mathrm{cm}^{-3}$, $r_c \simeq 1\,R_\odot$) and discuss the magnetic field and angular momentum of the formed protostar. The plan of the paper is as follows. The framework of our models are given in §2, the numerical method of our computations is shown in §3. The numerical results are presented in §4. We discuss the magnetic field and angular momentum of protostar, and compare our results with observations in §5.

2. Model

2.1. Basic Equations

To study the cloud evolution, we use the three-dimensional resistive MHD nested grid code. We solve the resistive MHD equations, including the self-gravity:

$$\frac{\partial \rho}{\partial t} + \nabla \cdot (\rho \boldsymbol{v}) = 0, \tag{1}$$

$$\rho \frac{\partial \boldsymbol{v}}{\partial t} + \rho(\boldsymbol{v} \cdot \nabla)\boldsymbol{v} = -\nabla P - \frac{1}{4\pi}\boldsymbol{B} \times (\nabla \times \boldsymbol{B}) - \rho \nabla \phi, \tag{2}$$

$$\frac{\partial \boldsymbol{B}}{\partial t} = \nabla \times (\boldsymbol{v} \times \boldsymbol{B}) + \eta \nabla^2 \boldsymbol{B}, \tag{3}$$

$$\nabla^2 \phi = 4\pi G \rho, \tag{4}$$

where ρ, $\boldsymbol{v}$, P, $\boldsymbol{B}$, η and ϕ denote the density, velocity, pressure, magnetic flux density, resistivity, and gravitational potential, respectively. To mimic the temperature evolution calculated by Masunaga & Inutsuka (2000), we adopt the piece-wise polytropic equation of state:

$$P = \begin{cases} c_s^2 \rho & \rho < \rho_c, \\ c_s^2 \rho_c \left(\frac{\rho}{\rho_c}\right)^{7/5} & \rho_c < \rho < \rho_d, \\ c_s^2 \rho_c \left(\frac{\rho_d}{\rho_c}\right)^{7/5} \left(\frac{\rho}{\rho_d}\right)^{1.1} & \rho_d < \rho < \rho_e, \\ c_s^2 \rho_c \left(\frac{\rho_d}{\rho_c}\right)^{7/5} \left(\frac{\rho_e}{\rho_d}\right)^{1.1} \left(\frac{\rho}{\rho_e}\right)^{5/3} & \rho > \rho_e, \end{cases} \tag{5}$$

where $c_s = 190\,\mathrm{m\,s^{-1}}$, $\rho_c = 3.84 \times 10^{-13}\,\mathrm{g\ cm^{-3}}$ ($n_c = 10^{11}\,\mathrm{cm^{-3}}$), $\rho_d = 3.84 \times 10^{-8}\,\mathrm{g\ cm^{-3}}$ ($n_d = 10^{16}\,\mathrm{cm^{-3}}$), and $\rho_e = 3.84 \times 10^{-3}\,\mathrm{g\ cm^{-3}}$ ($n_e = 10^{21}\,\mathrm{cm^{-3}}$). For convenience, we define 'the protostar formation epoch' as that at which the central density (n_c) reaches $n_\mathrm{c} = 10^{21}\,\mathrm{cm^{-3}}$. We also call the period for which $n_c < 10^{11}\,\mathrm{cm^{-3}}$ 'the isothermal phase', the period for which $10^{11}\,\mathrm{cm^{-3}} < n_\mathrm{c} < 10^{16}\,\mathrm{cm^{-3}}$ 'the adiabatic phase', the period for which $10^{16}\,\mathrm{cm^{-3}} < n_\mathrm{c} < 10^{21}\,\mathrm{cm^{-3}}$ 'the second collapse phase', and the period for which $n_\mathrm{c} > 10^{21}\,\mathrm{cm^{-3}}$ 'the protostellar phase,' respectively.

In this paper, a spherical cloud with a critical Bonnor-Ebert (Ebert 1955; Bonnor 1956) density profile, ρ_BE, is adopted as the initial condition. Initially the cloud rotates rigidly (Ω_0) around the z-axis and has a uniform magnetic field (B_0) parallel to the z-axis (or rotation axis). To promote contraction, we increase the density by a factor f (density enhancement factor) as

$$\rho(r) = \begin{cases} \rho_\mathrm{BE}(r)\, f & \text{for } r < R_c, \\ \rho_\mathrm{BE}(R_c)\, f & \text{for } r \geq R_c, \end{cases} \tag{6}$$

where r and R_c denote the radius and the critical radius for a Bonnor-Ebert sphere, respectively. We adopt the density enhancement factor as $f = 1.2$ or 1.4 (see Table 1) [1]. We assume $\rho_\mathrm{BE}(0) = f \times 3.841 \times 10^{-20}\,\mathrm{g\ cm^{-3}}$, which corresponds to a central number density of $n_{c,0} = f \times 10^4\,\mathrm{cm^{-3}}$. Thus, the critical radius for a Bonnor-Ebert sphere $R_c = 6.45\, c_s [4\pi G \rho_{BE}(0)]^{-1/2}$ corresponds to $R_c = 4.58 \times 10^4\,\mathrm{AU}$ for our settings. The initial model is characterized by three nondimensional parameters: α, ω, and c_η. The magnetic field strength and rotation rate are scaled using a central density $\rho_0 = \rho_\mathrm{BE}(0) f$ as

$$\alpha = B_0^2/(4\pi\, \rho_0\, c_s^2), \tag{7}$$

[1] The density enhancement factor is related to the stability of the initial cloud. The cloud is more unstable with larger f. We choose comparatively stable clouds in this paper. However, the cloud evolutions hardly depend on the value of f (for detail see Machida et al. 2006a).

and

$$\omega = \Omega_0/(4\pi\, G\, \rho_0)^{1/2}. \tag{8}$$

The parameter c_η represents the degree of the resistivity (for detail, see next section). We calculated 33 models by combining above parameters, which are listed in Table 1. The model parameters (α, ω, and c_η); density enhancement factor (f); magnetic field (B_0); angular velocity (Ω_0); total mass (M) inside the critical radius ($r < R_{\rm c}$); ratio of the thermal (α_0), rotational (β_0), and magnetic (γ_0) energies to the gravitational energy[2] are summarized in this table.

2.2. Resistivity and Magnetic Reynolds Number

We estimate the resistivity (η) according to Nakano et al. (2002). We assume that the resistivity is a function of the density and temperature. The temperature is a function of the density in our study, because we assume a barotropic equation of state. The resistivity (η) can be therefore expressed as a function of density, and is represented by a thick line in Figure 1. To investigate the effect of Ohmic dissipation (or dependence on the value of the resistivity), we parameterize the maximum value of the resistivity (η) keeping the shape of the function, and define c_η as

$$\eta = c_\eta\, \eta_0(\rho), \tag{9}$$

where $\eta_0(\rho)$ is a function of central density, and corresponds to the thick line in Figure 1. The resistivity (η) corresponds to $\eta_0(\rho)$ when we choose $c_\eta = 1$. In this paper, we adopted $c_\eta = 0, 10^{-3}, 0.01, 0.1, 1,$ and 10 as listed in Table 1. Since the second term on the right-hand side in equation (3) is vanished in models with $c_\eta = 0$, these models obey to the ideal MHD approximation. In this paper, we call models having $c_\eta \neq 0$ 'the non-ideal MHD model ', and models having $c_\eta = 0$ 'the ideal MHD model.'

We analytically estimate the magnetic Reynolds number for models with different c_η ($Re \equiv v_f\, \lambda_j\, \eta^{-1}$; thin lines in Fig. 1), where $v_f \equiv [(4/3)\pi G \lambda_j^2 \rho_c]^{1/2}$ is the free-fall velocity and $\lambda_j \equiv (\pi c_s^2/G\rho_c)^{1/2}$ is the Jeans length. The magnetic dissipation is effective during $2\times10^{12}\,{\rm cm}^{-3} \lesssim n_c \lesssim 6\times10^{15}\,{\rm cm}^{-3}$ in models with $c_\eta = 1$ (thin solid line) which corresponds to the results of Nakano et al. (2002), while it is effective during $2\times10^{14}\,{\rm cm}^{-3} \lesssim n_c \lesssim 2\times10^{15}\,{\rm cm}^{-3}$ in models with $c_\eta = 0.01$.

---

[2] Denoting the thermal, rotational, magnetic, and gravitational energies as U, K, M, and W, the relative factors against the gravitational energy are defined as $\alpha_0 = U/|W|$, $\beta_0 = K/|W|$, and $\gamma_0 = M/|W|$.

3. Numerical Method

We adopt the nested grid method (for detail, see Machida et al. 2005a, 2006a) to obtain high spatial resolution near the center. Each level of a rectangular grid has the same number of cells ($= 64 \times 64 \times 32$), although the cell width $h(l)$ depends on the grid level l. The cell width is reduced by a factor 1/2 as the grid level increases by 1 ($l \rightarrow l + 1$). We assumed mirror symmetry with respect to z=0. The highest level of grids changes dynamically. We begin our calculations with four grid levels ($l = 1, 2, 3, 4$). Box size of the initial finest grid $l = 4$ is chosen equal to be $2R_{\rm c}$, where R_c denotes the radius of the critical Bonnor-Ebert sphere. The coarsest grid ($l = 1$), therefore, has a box size equal to $2^4\,R_{\rm c}$. A boundary condition is imposed at $r = 2^4\,R_{\rm c}$, where the magnetic field and ambient gas rotate at an angular velocity of Ω_0 (for detail, see Matsumoto & Tomisaka 2004). A new finer grid is generated whenever the minimum local Jeans length $\lambda_{\rm J}$ becomes smaller than $8\,h(l_{\rm max})$, where h is the cell width. The maximum level of grids is restricted to $l_{\rm max} = 30$. Since the density is highest in the finest grid, the generation of a new grid ensures the Jeans condition of Truelove et al. (1997) with a margin of a safety factor of 2. We adopted the hyperbolic divergence $\boldsymbol{B}$ cleaning method of Dedner et al. (2002).

4. Results

Starting from the number density $n_{\rm c} = f \times 10^4\,{\rm cm}^{-3}$ ($f = 1.2$ or 1.4), we calculate the cloud evolution until the protostar is formed ($n_{\rm c} \simeq 10^{22}\,{\rm cm}^{-3}$). We assume that initial clouds have the magnetic field of $B_0 = 0-34\,\mu{\rm G}$, and the angular velocity of $\Omega_0 = 0-3.1\times10^{-14}{\rm s}^{-1}$ as listed in Table 1. These values are comparable to the observed magnetic field (Crutcher 1999) and angular velocity (Goodman et al. 1993; Caselli 2002) of the molecular cloud cores. Figure 2 shows the evolution of the magnetic field ($B_{\rm c}$) and angular velocity (Ω_c) at the center of the cloud for Models 3, 8, 16, 22, and 23. The growth rates of the magnetic field for the non-ideal MHD models ($c_\eta \neq 0$; Models 16, 22, 23) are smaller than that for the ideal MHD models ($c_\eta \neq 0$; Models 3, 8) during $10^{11}\,{\rm cm}^{-3} \lesssim n_{\rm c} \lesssim 10^{16}\,{\rm cm}^{-3}$ (Fig. 2 upper panel). This is because the magnetic field is effectively dissipated by Ohmic dissipation for this phase. The magnetic fields ($B_{\rm f}$) at the star formation epoch ($n_{\rm c} \simeq 10^{21}\,{\rm cm}^{-3}$) are denoted in the 12th column of Table 1. Models with $c_\eta = 0$ (the ideal MHD models) have the magnetic field of $\sim 100\,{\rm kG}$ (106 kG: Model 3, 67.3 kG: Model 8), while models with $\eta \neq 0$ (the non-ideal MHD models) have the magnetic field of 0.1-1 kG (0.11 kG: Model 16, 0.68 kG: Model 22, and 0.32 kG: Model 23). The magnetic field strengths of protostars observed from Zeeman broadening measurement are $\sim 1\,{\rm kG}$ (Johns-Krull et al. 1999a,b, 2001; Bouvier 2006). Even though the protostars in the non-ideal MHD models have only

mass of $\sim 10^{-3}\,M_\odot$ in our simulation, they have equivalent magnetic field strengths to the observed protostars. The magnetic field is considered to be amplified for magneto-rotational instability (MRI; Balbus & Hawley 1991) and convection on the surface of protostar in the later phase. However, our results indicate that the protostar already have the magnetic field of $\sim$kG for the non-ideal MHD models at their formation epoch. On the other hand, when protostar is formed, the magnetic field for the ideal MHD models reaches $B \sim$100 kG, which is about 100 times larger than the magnetic field of observed protostars.

The rotation periods (P) at the star formation epoch ($n_{\rm c} \simeq 10^{21}\,{\rm cm}^{-3}$) are denoted in the 13th column of Table 1. The evolutions of the angular velocity ($\Omega_{\rm c}$; left axis) and the rotation period (P; right axis) at the center of the cloud are shown in Figure 2 lower panel. This figure shows that the rotation periods reach P=1–100 days at the protostar formation epoch ($n_{\rm c} = 10^{21}\,{\rm cm}^{-3}$) even when the initial cloud has rather small angular velocity ($2\times10^{-17}{\rm s}^{-1}$). Many observations indicate that the protostars have the rotation periods of P = 0.6–20 days (e.g., Herbst et al. 2006). Thus, the rotation periods derived from our calculation are roughly agreement with those from observed protostars. The angular momentum is considered to be modified by the interaction between the protostar and protoplanetary disk, jets and outflows in later phase of star formation. However, in our calculations, the protostars have the same orders of magnitude of rotation rate at their formation epoch as well as the magnetic field.

We show the evolution of the magnetic field in the collapsing cloud in the following sections in detail. Firstly, we show the cloud evolution for the ideal MHD models ($c_\eta = 0$) to simply investigate the evolution of the magnetic field. The cloud evolution for the non-ideal MHD models ($c_\eta \neq 0$) are shown in subsequent sections.

4.1. The Evolution of the Magnetic Field for the Ideal MHD Model

Figure 3 shows the evolution of the magnetic field ($B_{\rm c}$) normalized by the square root of the density ($\rho_{\rm c}^{1/2}$) at the center of the cloud for the ideal MHD models ($\eta = 0$). As shown in Machida et al. (2005a, 2006a), the evolution of $B_{\rm c}/\rho_{\rm c}^{1/2}$ depends on the mode of the cloud collapse (spherical, vertical or disk-like collapse). When the cloud has a small amount of the rotational and magnetic energy, the cloud collapses almost spherically (spherical collapse). On the other hand, the cloud collapses vertically along the rotation axis or magnetic field lines (vertical collapse), when the cloud has a large amount of the rotational or magnetic energy. In either case, a thin disk finally forms around the center of cloud, and the cloud continues to collapse keeping disk-like structure (disk-like collapse) in both case of the spherical and vertical collapse. We briefly summarize the relation of the growth rate of the central

magnetic field and the cloud density (for detail see Machida et al. 2005a, 2006a). The magnetic field strength increases as $B_{\rm c} \propto \rho_{\rm c}^{2/3}$ in the weakly magnetized and slowly rotating clouds (spherical collapse), because the cloud evolution are mainly controlled by the thermal pressure and gravity. The magnetic field keeps a constant value as $B_{\rm c} \propto \rho_{\rm c}^{0}$ when the cloud is magnetized strongly or rotating rapidly (vertical collapse), because the radial contraction of the cloud is suppressed by the strong magnetic tension or centrifugal force. After the disk formation, the magnetic field evolves as $B_{\rm c} \propto \rho_{\rm c}^{1/2}$, and the Lorentz and centrifugal forces are balanced with the thermal pressure gradient and gravitational forces in the collapsing cloud (disk-like collapse) [3]. For the isothermal phase ($n_{\rm c} \lesssim 10^{11}\,{\rm cm}^{-3}$), the value of $B/\rho^{1/2}$ at the center of the cloud are converged to a certain value (Magnetic Flux-Spin relation; Machida et al. 2005a) when the cloud have a smaller rotational energy than the magnetic energy at the initial state. Thus, the initial strength of the magnetic field is not sensitive to the cloud evolution especially in $n_{\rm c} > 10^{11}\,{\rm cm}^{-3}$ if the field strength is strong enough. The observations indicate that the magnetic energy is much larger than the rotational energy in molecular cloud cores (Crutcher 1999; Caselli 2002). Thus, this convergence of $B/\rho^{1/2}$ is expected in the collapsing region of the real molecular clouds.

Figure 3 upper panel shows the evolutions of the magnetic field in non-rotating clouds ($\omega = 0$) having different magnetic fields at the initial stage (Models 1, 2, 3, 4, 5, and 6). In these models, the magnetic field of Model 1 ($B_0 = 34\,\mu$G) has about 70 times stronger than that of Model 6 ($B_0 = 0.5\,\mu$G) at the initial stage. We can see from Figure 3 upper panel that the magnetic fields for all models are converged into a certain value [$B_{\rm c}/\rho_{\rm c}^{1/2} \simeq 0.55$ (Model 6) – 1.2 (Model 12)] at the end of the isothermal phase ($n_{\rm c} \simeq 10^{11}\,{\rm cm}^{-3}$). The values $B_{\rm c}/\rho_{\rm c}^{1/2}$ begin to increase after the gas becomes adiabatically ($n_{\rm c} \gtrsim 10^{11}\,{\rm cm}^{-3}$), because the geometry of the collapse is changed from disk-like into spherical shape for increasing thermal pressure. However, the clouds at these snapshots have almost the same magnetic field strengths for this epoch ($n_{\rm c} \gtrsim 10^{11}\,{\rm cm}^{-3}$), because the growth rates of the magnetic field are almost the same for these models. The formed protostars have the magnetic field of $B_{\rm c} = 88.9 - 123\,{\rm kG}$ at the protostar formation epoch ($n_{\rm c} \simeq 10^{21}\,{\rm cm}^{-3}$) as listed in Table 1. Thus, the formed protostars have only 1.4 times different strength of the magnetic field, while clouds have 70 times different strength of the magnetic field at the initial stage. As a result, the protostars formed from initially non-rotating clouds have almost the same magnetic field if Ohmic dissipation is ignored. As shown in later sections, since both of the cloud rotation and Ohmic dissipation only decrease the magnetic field strength of the formed protostar, the protostar at its formation epoch cannot have the magnetic field exceeding $B_{\rm c} \simeq 100\,{\rm kG}$

[3] In this paper, we use the terminology 'disk-like collapse' when the disk is formed and the magnetic field increases as $B_{\rm c} \propto \rho_{\rm c}^{1/2}$ at the center of the cloud.

which derived from the non-rotating and the ideal MHD models.

The growth rate of the magnetic field depends on the cloud rotation when the initial clouds have the same magnetic fields, because the geometry of the collapse depends not only on the magnetic field but also on the cloud rotation (Machida et al. 2005a, 2006a). Figure 3 lower panel shows the evolution of the magnetic field strength normalized by square root of the density ($B_{\rm c}/\rho_{\rm c}^{1/2}$) for the ideal MHD models ($c_\eta = 0$) with different initial angular velocities and the same initial magnetic field strengths ($B_{\rm c} = 1.6\,\mu$G). This figure indicates that the growth rate of the magnetic field is smaller for initially rapid rotating cloud. Noted that we stopped calculation at $n_{\rm c} \simeq 10^{12}\,{\rm cm}^{-3}$ in Model 11, because fragmentation occurs in this model that have the largest angular velocity at the initial state. At the protostar formation epoch ($n_{\rm c} = 10^{21}\,{\rm cm}^{-3}$), cloud with initially slowest angular velocity ($\omega = 0.001$; Model 7) has the magnetic field of $B_{\rm c} = 95.9\,$kG, while rapidly rotating cloud with $\omega = 0.1$ (Model 10) has $B_{\rm c} = 43.7\,$kG (Table 1). This is because the growth rate of the magnetic field changes from $B \propto \rho^{2/3}$ to $B \propto \rho^{1/2}$ at earlier evolutional stage in more rapidly rotating cloud. Therefore, the magnetic field at the protostar formation epoch depends on the rotation of the initial cloud. However, a slowly rotating cloud has only twice strength of the magnetic field compared with a rapidly rotating cloud (see Models 7-11 in Table 1).

Figure 4 shows the cloud evolution from the initial state ($n_{\rm c} = 1.4 \times 10^4\,{\rm cm}^{-3}$; Fig. 4*a*) to the protostar formation epoch. ($n_{\rm c} = 4.4 \times 10^{21}\,{\rm cm}^{-3}$; Fig. 4) for Model 12. Model 12 has parameters of $\alpha = 0.01$, $\omega = 0.01$, and $c_\eta = 0$. In this model, the magnetic field is well coupled with the gas from the initial to the final stage because of $c_\eta = 0$ (the ideal MHD model). The initial cloud is weakly magnetized ($B_0 = 1.4\,\mu$G) and rotating slowly ($\Omega_0 = 2 \times 10^{15}\,{\rm s}^{-1}$). This cloud is classified into magnetic-force dominant models by the criterion represented in Machida et al. (2005a, 2006a), because the ratio of the initial angular velocity(Ω_0) to the magnetic field (B_0) is $\Omega_0/B_0 = 1.4 \times 10^{-9} < 5.3 \times 10^{-9} \equiv (\Omega/B)_{\rm cri}$. Thus, the magnetic field affects the cloud evolution, while the cloud rotation hardly affects the cloud evolution (for detail, see Machida et al. 2005a, 2006a). Figure 5 shows the magnetic field distribution at the same epoch of each panel in Figure 4. As shown in Figure 4*a* and *b*, the central region becomes gradually oblate as the cloud collapses, and a thin disk is formed in the isothermal phase ($n_{\rm c} \lesssim 10^{11}\,{\rm cm}^{-3}$). The magnetic field lines are gradually converged towards the center (Fig. 5*b* and *c*). This configuration of the magnetic field lines are similar to those observed by Girart et al. (2006). Thin solid lines in Figure. 6 left panels show the evolution of the magnetic field normalized by the square root of the density ($B_{\rm c}/\rho_{\rm c}^{1/2}$; Fig. 6*a*), plasma beta ($\beta_{\rm p} \equiv 8\pi c_s^2/B_{\rm c}^2$; Fig. 6*b*), and specific angular momentum normalized by the mass (J/M^2; Fig. 6*c*) within the region of $\rho > 0.1\rho_c$ against the central density. Figure 6*a* and *b* show that both of the values of $B_{\rm c}/\rho_{\rm c}^{1/2}$ and J/M^2 continue to increase for the isothermal phase ($n_{\rm c} \lesssim 10^{11}\,{\rm cm}^{-3}$). Thus, it is considered

that the disk is formed by the Lorentz and centrifugal forces as shown in Figure 5*c* (color and contours on the wall). The plasma beta has a minimum of $\beta_{\rm p} \simeq 8$ at the end of the isothermal phase ($n_{\rm c} \simeq 10^{11}\,{\rm cm}^{-3} - 10^{12}\,{\rm cm}^{-3}$; Fig. 6 middle panel). Even after the gas around the center of the cloud becomes adiabatic ($n_{\rm c} \gtrsim 10^{11}\,{\rm cm}^{-3}$), the magnetic field continues to be amplified (Fig. 6*a*). On the other hand, the plasma beta keeps $\beta_{\rm p} \simeq 10 - 20$ during $n_{\rm c} \gtrsim 10^{17}\,{\rm cm}^{-3}$, after it increases slightly owing to the increase of the thermal energy during $10^{12}\,{\rm cm}^{-3} \lesssim n_{\rm c} \lesssim 10^{16}\,{\rm cm}^{-3}$.

When the gas reaches $n_{\rm c} \simeq 10^{11}\,{\rm cm}^{-3}$, the central region becomes optically thick and the equation of state becomes hard as derived from the one-dimensional radiative hydrodynamical calculation (Masunaga & Inutsuka 2000). After the equation of state becomes hard, the shock occurs and the first core is formed. The first core is formed at $n_{\rm c} \sim 10^{13}\,{\rm cm}^{-3}$ in this model. The first core is shown by a white-dotted line in Figure 4*c* and *d* (We plot the position where the shock is occurred on $z = 0$ plane in these panels). The first core has mass of $\sim 0.012\,M_\odot$ and radius of $\sim 7\,{\rm AU}$. Arrows in Figure 4*d* indicate that the radial component of the velocity ($v_{\rm r}$) is dominant outside the first core, while the azimuthal component of the velocity (v_ϕ) is comparable to the radial one inside the first core on $z = 0$ plane. This is because the large thermal pressure suppresses the cloud collapse inside the first core, thus the rotation timescale becomes smaller than the collapse one. We can see from Figure 4*d* lower panel that the outflow is driven from the first core.[4] The outflow appears when the central density reaches $n_{\rm c} \simeq 10^{15}\,{\rm cm}^{-3}$. The outflows driven from the first cores are also shown by Tomisaka (2002), Matsumoto & Tomisaka (2004), Machida et al. (2005b), and Banerjee & Pudritz (2006). As shown in Figure 5*d*, the magnetic field lines begin to twist due to the rotation of the first core. This outflow reaches $\sim 10\,{\rm AU}$ and has the maximum speed of $\sim 3\,{\rm km\,s}^{-1}$ at the end of the calculation.

The specific angular momentum normalized by the mass (J/M^2) begins to decrease for the adiabatic phase. Matsumoto et al. (1997) and Saigo & Tomisaka (2006) show that after this value reaches a peak in the unmagnetized clouds, the value J/M^2 keeps a constant value. Thus, the decrease of J/M^2 is caused by the magnetic effect. Since no outflow appears before the first core formation, the decrease of J/M^2 for this phase is caused by the magnetic braking (Basu & Mouschovias 1994). After the central density reaches $n_{\rm c} \simeq 10^{15}\,{\rm cm}^{-3}$, the value of J/M^2 decreases more intensely. This indicates that the angular momentum is removed by not only the magnetic braking but also the outflow for the adiabatic phase. Tomisaka (1998) and Matsumoto & Tomisaka (2004) show that the outflow is important mechanism for the angular momentum transfer.

[4] For convenience, we call the flow driven from the first core 'the outflow', and the flow driven from the second core 'the jet' in this paper.

The cloud collapses again inside the first core for $10^{16}\,\mathrm{cm}^{-3} \lesssim n_\mathrm{c} \lesssim 10^{21}\,\mathrm{cm}^{-3}$, because of the dissociation of the molecule hydrogen (i.e., second collapse). Then, the equation of state becomes hard again and the second core (i.e., protostar) is formed at $n_\mathrm{c} \simeq 10^{21}\,\mathrm{cm}^{-3}$ (Masunaga & Inutsuka 2000). Figure 4*e* shows the structure near the protostar (the protostar or shocked region is represented by a black-dotted line). The gas around protostar has the density range of $10^{17}\,\mathrm{cm}^{-3} \lesssim n_\mathrm{c} \lesssim 10^{20}\,\mathrm{cm}^{-3}$ and collapses intensely, because the equation of state is soft in this region [see eq.(5)]. Thus, the gas accretes onto the protostar with high speed of $\sim 10\,\mathrm{km\,s}^{-1}$. Since the rotation velocity is comparable to the accretion velocity, the magnetic field lines are strongly twisted (Fig.5*d*). Figure 4*f* shows the structure around the protostar 215 hours after the protostar formation epoch. The protostar has mass of $2.1 \times 10^{-3}\,M_\odot$ and radius of $1.1\,R_\odot$ at this epoch. The disk surrounded by protostar extends up to $3.9\,R_\odot$ having $1.2 \times 10^{-4}\,M_\odot$. The strong jet is driven from the protostar as shown in Figure 4*f* upper panel. The jet driven from the protostar is also shown by Tomisaka (2002), Banerjee & Pudritz (2006), and Machida et al. (2006b). The jet reaches $11\,R_\odot$ at the end of the calculation. In this model, since the effect of Ohmic dissipation is ignored ($c_\eta = 0$; the ideal MHD model), the magnetic field couple with the gas at any time. Thus, the magnetic field around the protostar strongly twisted at the protostar formation epoch as shown in Figure 5*f*. The cloud evolution of Model 12 is well similar to that in Tomisaka (2002) and Banerjee & Pudritz (2006), in which they studied the evolution of the magnetized cloud in ideal MHD regime.

4.2. Evolution of Magnetic Field in Non-Ideal MHD Model

Figure 7 and 8 show the cloud evolution for Model 16. Model 16 has the same magnetic field strength ($\alpha = 0.01$, $B_0 = 1.4\,\mu$G) and angular velocity ($\omega = 0.01$, $\Omega_0 = 1.4\times10^{-14}\mathrm{s}^{-1}$) as Model 12 (Fig. 4 and 5) at the initial state. However, Model 16 has the parameter of $c_\eta = 1$, which means that the magnetic field is dissipated by Ohmic dissipation in the collapsing cloud (the non-ideal MHD model), while the effect of Ohmic dissipation is ignored in Model 12 ($c_\eta = 0$; the ideal MHD model). In Model 16, the magnetic Reynolds number becomes $Re < 1$ during $2 \times 10^{12}\,\mathrm{cm}^{-3} \lesssim n_\mathrm{c} \lesssim 6 \times 10^{15}\,\mathrm{cm}^{-3}$ (Fig. 1). Thus, the cloud evolutions of Models 12 and 16 are almost the same for $n_\mathrm{c} \ll 10^{12}\,\mathrm{cm}^{-3}$, because Ohmic dissipation is not effective even in Model 16 for this early phase. The magnetic field normalized by the square root of the density ($B/\rho^{1/2}$), plasma beta (β_p), and specific angular momentum normalized by mass (J/M^2) in Model 16 (thick solid lines in Fig. 6*a*-*c*) are completely the same as those in Model 12 (thin solid lines in Fig. 6*a*-*c*) during $n_\mathrm{c} \lesssim 10^{11}\,\mathrm{cm}^{-3}$. Thus, we plotted the cloud evolution for Model 16 in Figure 7 and 8 only after the first core is formed.

The first core is formed at $n_{\rm c} \simeq 10^{13}\,{\rm cm}^{-3}$ in Model 16 as well as Model 12. Figure 7*a* and Figure 4*c* show that the first cores in Models 12 and 16 have almost the same shape and size. The first core has the mass of $0.012\,M_\odot$ and the radius of 7 AU in Model 16. As shown in Figure 8*a*, the poloidal component of the magnetic field is dominant at the first core formation epoch ($n_{\rm c} \simeq 10^{13}\,{\rm cm}^{-3}$). After the first core formation, the magnetic field lines begin to be twisted (Fig. 8*b*).

Outflow driven from the first core is seen in Figure 7*c* lower panel (red-solid lines). Outflow appeared 22 yr after the first core formation epoch in Model 16 ($n_{\rm c} \simeq 10^{17}\,{\rm cm}^{-3}$), while outflow appeared 2.6 yr after the first core formation epoch ($n_{\rm c} \simeq 10^{15}\,{\rm cm}^{-3}$) in Model 12. In Model 16, outflow has the maximum speed of $\sim 2\,{\rm km\,s}^{-1}$ and reaches ~ 1 AU at the end of the calculation. Figure 7*c* and Figure 4*d* show that outflow in Model 16 has smaller scale and slower speed than those in Model 12. The outflow is mainly driven by the Lorentz force in the region outside the first core. The magnetic field is weak and hardly twisted around the first core in Model 16, because the magnetic field in this region is dissipated by Ohmic dissipation. Thus, outflow in the non-ideal MHD model (Model 16) is weaker than that in the ideal MHD model (model 12). We will discuss further the driving mechanism of outflow and jet in a companion paper.

Figure 6*a* shows that the magnetic field in Model 16 (thick-solid line) is largely removed from the central region during $10^{12}\,{\rm cm}^{-3} \lesssim n_{\rm c} \lesssim 10^{16}\,{\rm cm}^{-3}$. The plasma beta in Model 16 increases from $\beta_{\rm p} \simeq 10$ to $\simeq 2 \times 10^5$ for the same epoch (Fig. 6*b*). In Figure 8*c*, the magnetic field lines are strongly twisted near the center of the cloud, while they are hardly twisted in the region away from the center of the cloud. This implies that the neutral gas is well coupled with the magnetic field, and the magnetic field lines rotate with the neutral gas near the center, because Ohmic dissipation is ineffective. When the gas density reaches $n_{\rm c} \simeq 10^{16}\,{\rm cm}^{-3}$, the temperature reaches $T \sim 2000$K. Thus, the thermal ionization of Alkali metals reduces the resistivity, and Ohmic dissipation becomes ineffective. As a results, the magnetic field is coupled with the gas and amplified again for $n_{\rm c} \gtrsim 10^{16}\,{\rm cm}^{-3}$. On the other hand, the neutral gas is decoupled from the magnetic field in the region away from the center and the magnetic field lines slip through the neutral gas and rotate freely, because this region has the density range of $10^{11}\,{\rm cm}^{-3} \lesssim n_{\rm c} \lesssim 10^{15}\,{\rm cm}^{-3}$ (Figure 7*c* lower panel) and the magnetic dissipation is effective. Thus, the magnetic field lines that are strongly twisted once in the earlier phase ($n_{\rm c} \ll 10^{12}\,{\rm cm}^{-3}$) are de-collimated and relaxed by the magnetic tension force. Note that the magnetic field lines do not disappear even with Ohmic dissipation. In our settings, the existence of the vertical component of the magnetic field ($B_{\rm z}$) is assumed in the initial state. Thus, even when both of the azimuthal (B_ϕ) and radial ($B_{\rm r}$) component of the magnetic field are completely dissipated by Ohmic dissipation, the vertical component of the magnetic field remains because of the condition of $\boldsymbol{\nabla} \cdot \boldsymbol{B} = 0$.

As shown in the upper panel of Figure 7*d*, the gas inside the first core is rotating rapidly. The specific angular momentum in Model 16 is larger than that in Model 12 (Fig. 6*c*) for $n_{\rm c} \gtrsim 10^{12}\,{\rm cm}^{-3}$, while the magnetic field in Model 16 is smaller than that in Model 12 (Fig. 6*a*). This means that the magnetic braking is less effective in Model 16 for the weak magnetic field. Therefore, a strong centrifugal force make a thin disk at the center of cloud as shown by projected density contour on the sidewall in Figure 8*d* and *e*. In addition, the cloud collapses slowly for the rapid rotation as discussed in Saigo & Tomisaka (2006). It takes 40.7 yr to form the second core ($n_{\rm c} \simeq 10^{21}\,{\rm cm}^{-3}$) from the first core formation epoch ($n_{\rm c} \simeq 10^{13}\,{\rm cm}^{-3}$) in Model 16, while it takes 25.5 yr in Model 12. The magnetic field lines begin to be twisted again inside the first core (Fig. 8*d* and *e*). Then, another flow different from the outflow driven from the first core appears as shown in lower panels in Figure 7*d* and *e*. Inside the red line in Figure 7*d* lower panel, the slow flows (i.e., the outflow) driven from the first core are seen in the region of $|z| > 0.4$, while the fast flows (i.e., the jet) driven from a rotational supported core inside the first core are seen in the region of $|z| < 0.4$.

To investigate the property of the outflow and jet, we show the z-component of the velocity (v_z; upper side), and plasma beta ($\beta_{\rm p}$; lower side) in Figure 9 at the same epoch and with the same scale as Figure 7*d*. In this figure, we can see two peaks of z-component of the velocity (outer weak, and inner strong peaks; Fig. 9 upper side). Outer weak peaks with $v_z \simeq 5\,{\rm km\,s}^{-1}$ are located at (x, z) = (± 0.3, 0.3), and are originated from the first core. On the other hand, the inner strong peaks with $v_z \simeq 15\,{\rm km\,s}^{-1}$ are located at (x, z) = (± 0.05, 0.3), and are originated from the rotation supported quasi-static core inside the first core. In the upper panel, we labeled 'outflow' as the flow driven from the first core, and 'jet' as the flow driven from the quasi-static core. Figure 9 lower panel shows that the plasma beta is $\beta_{\rm p} < 1$ in the regions around the velocity peak, which indicates that flows with $v_z > 0$ ($v_z < 0$) for $z > 0$ ($z < 0$) are driven from the region with strong magnetic field. These regions are composed of the low-density gas ($n_{\rm c} \lesssim 10^{13}\,{\rm cm}^{-3}$) as shown in Figure 7*d*, thus Ohmic dissipation is ineffective (Fig. 1) and the magnetic field can be amplified as the cloud collapses. On the other hand, the central object and disk located in $z < |0.1|$ have a large plasma beta ($\beta_{\rm p} = 10^5 - 10^7$), because Ohmic dissipation is effective in this region. The jet is driven from the second core (i.e., protostar) after the protostar formation epoch ($n_{\rm c} = 10^{21}\,{\rm cm}^{-3}$) in Model 12, while the jet is driven from the quasi-static core before the protostar formation epoch in Model 16. This is because the rotation supported core is formed before central density reaches $n_{\rm c} = 10^{21}\,{\rm cm}^{-3}$ in Model 16 owing to less effective magnetic braking. Figure 7*e* shows the cloud structure when the density reaches $n_{\rm c} = 8.1 \times 10^{18}\,{\rm cm}^{-3}$. In this figure, strong jet is driven from the center.

When the gas density reaches $n_{\rm c} \simeq 1.3 \times 10^{21}\,{\rm cm}^{-3}$ in Model 16, the shock is occurred near the center of the cloud and the protostar (i.e., second core) is formed. The protostar

in Model 16 is formed at lower density than that in Model 12. The protostar has the mass of $9.1 \times 10^{-4}\,M_\odot$, and the radius of $3\,R_\odot$ at its formation epoch. The radius of protostar in Model 16 is three times larger than that in Model 12. The central region inside the first core rotates rapidly in Model 16, thus, a considerably flattened disk (Fig. 7*f* lower panel) is formed near the center for the strong centrifugal force. Figure 7*f* and Figure 4*f* show that the protostar in Model 16 is rotating rapidly and has a more oblate structure. Figure 8*f* shows that the magnetic field lines are weakly twisted around protostar, where Ohmic dissipation is effective. This is because the rapidly rotation makes the first core (or high-density region) more and more oblate as the cloud evolves, and the region above and below the protostar (or the first core) have low-density gases ($n_{\rm c} \lesssim 10^{15}\,{\rm cm}^{-3}$) as shown in Figure 7*f* lower panel. Thus, the magnetic field is decoupled from the neutral gas, and de-collimated again in this region.

As a result, Ohmic dissipation affects not only the distribution and strength of the magnetic field but also the cloud collapse, rotation, outflow, and jet.

4.3. Dependence on c_η

Ohmic dissipation seriously influences the cloud evolution as denoted in previous section. As shown by a thick solid line in Figure 1, we estimate the resistivity as a function of the density and temperature according to Nakano et al. (2002). However, we should note that it is difficult to determine the ionization structure accurately, because there are uncertainties mainly in the properties of dust grains that provide the most important sites for recombination in the collapsing clouds. Thus, we parameterize the model of the magnetic dissipation (c_η), and investigate the cloud evolution as shown in Figure 6. Figure 6 left panels show the evolution of models with the same magnetic field and angular velocity ($\alpha = 0.01$ and $\omega = 0.01$) but different c_η. In Figure 6*a*, the magnetic field is removed from the cloud efficiently with larger c_η. Plasma beta keeps $\beta_{\rm p} \simeq 10 - 20$ for $n_{\rm c} \gtrsim 10^{12}\,{\rm cm}^{-3}$ in the ideal MHD model ($c_\eta = 0$; Model 12), while it reaches $\beta_{\rm p} \simeq 10^5$ for $10^{12} \lesssim n_{\rm c} \lesssim 10^{15}\,{\rm cm}^{-3}$ in Model 16 ($c_\eta = 1$) in Figure 6*b*. Thus, the central region in Model 12 has the magnetic energy $\sim 10^4$ times larger than that in Model 16. This difference of magnetic energy between Models 12 and 16 is caused by the Ohmic dissipation during $10^{12}\,{\rm cm}^{-3} \lesssim n_{\rm c} \lesssim 10^{16}\,{\rm cm}^{-3}$. The amount of the magnetic energy in the central region depends on c_η as shown in Figure 6*b*. In contrast, the angular momentum is large and the cloud rotates rapidly in model with larger c_η as shown in Figure 6*c*. This is because the magnetic braking is less effective in model with larger c_η for smaller amount of the magnetic energy. As a result, the protostar with larger c_η has a larger angular momentum at its formation epoch. In Model 17 ($c_\eta = 10$),

the cloud rotates rapidly and fragmentation occurs at $n_c \simeq 10^{19}\,\mathrm{cm}^{-3}$, because the magnetic energy is considerably small and the magnetic braking hardly works.

Figure 6 right panels (Fig. 6*d*-*f*) show the evolution of models having the same magnetic field ($\alpha = 0.01$) and rotation rate ($\omega = 10^{-4}$) with different c_η. At the initial state, the rotation rates in models appeared in Figure 6 right panels are 100 times smaller than those in left panels ($\omega = 10^{-2}$), while the magnetic field strengths are the same in both panels. The evolution of the magnetic field and plasma beta is almost the same for $n_c \lesssim 10^{15}\,\mathrm{cm}^{-3}$ in both panels of Figure 6*a* and *d*. After the magnetic dissipation, the evolutions in models appeared in left and right panels are mutually different. The value $B_c/\rho_c^{1/2}$ increase with the gas density for $n_c \gtrsim 10^{15}\,\mathrm{cm}^{-3}$ in Models 18–23 (Fig. 6*d*), while it keeps almost constant value in Models 12-17 (Fig. 6*a*). The magnetic field is more amplified in the spherical collapse ($B \propto \rho^{2/3}$) than in the disk-like collapse ($B \propto \rho^{1/2}$) as denoted in §4.1. In the ideal MHD model, even if the cloud has no angular momentum, the geometry of the collapse is changed from the spherical to the disk-like collapse, because the magnetic field is amplified and the disk-like structure is formed at the center of the cloud. After the disk-like structure is formed (i.e., disk-like collapse), the growth rate of the magnetic field becomes small (Machida et al. 2005a). However, if the magnetic field is removed from the central region sufficiently, the geometry of the collapse is changed from the disk-like to the spherical collapse again, and the magnetic field is amplified as $B \propto \rho^{2/3}$ (spherical collapse). In Models 18–21, after the dissipation of the magnetic field ($n_c \gtrsim 10^{16}\,\mathrm{cm}^{-3}$) , the clouds collapse spherically because of the extremely slow rotation, while clouds collapse with disk-like shape for the rapid rotation in Models 12–17. At the protostar formation epoch ($n_c \simeq 10^{21}\,\mathrm{cm}^{-3}$), the magnetic field is amplified to $B_c = 0.11\,\mathrm{kG}$ in Model 16 (rapidly rotating cloud), while it is amplified to $B_c = 0.68\,\mathrm{kG}$ in Model 22 (slowly rotating cloud). Thus, the protostar has a stronger magnetic field in more slowly rotating cloud even in the non-ideal MHD models. After the magnetic field is significantly removed from the center, the angular velocity is also amplified because the cloud collapses spherically. Thus, the specific angular momentum normalized by its mass (J/M^2) also increases in Models 18-23 (Fig. 6*f*), while J/M^2 has a constant value in more rapidly rotating cloud of Models 12-17 for the disk-like collapse (Fig. 6*c*).

4.4. Cloud Evolution with Different Angular Momentum

Figure 10 shows the evolution of the magnetic field ($B_c/\rho_c^{1/2}$; upper panel) and the angular velocity [$\Omega/(4\pi G\rho_c)^{1/2}$; lower panel] for Models 24–28. These models have the same magnetic field ($\alpha = 0.01$) and c_η ($c_\eta = 1$), but different angular velocity ω. In this figure, the circles indicate the fragmentation epoch. Fragmentation occurs in the rapidly rotating

cloud of Models 27 ($\omega = 0.03$) and 28 ($\omega = 0.1$). Machida et al. (2005b) shows that fragmentation occurs when the central angular velocity ($\Omega_{\rm c}$) normalized by free-fall timescale $[1/(4\pi\, G\, \rho_{\rm c})^{1/2}]$ reaches $\Omega_{\rm c}/(4\pi {\rm G}\rho)^{1/2} \simeq 0.2$ for the isothermal phase ($n_{\rm c} \lesssim 10^{11}\,{\rm cm}^{-3}$). As shown in Figure 10 lower panel, this condition is realized in Models 27 and 28. After fragmentation occurs, we stopped calculation because our numerical code (nested grid) is not suitable for calculating the evolution of each fragment located out of the center. The protostar is formed without fragmentation in Models 24, 25, and 26, because the fragmentation condition is not realized in these clouds as shown in Figure 10 lower panel.

Figure 10 upper panel shows the evolution of the magnetic field ($B_{\rm c}/\rho_{\rm c}^{1/2}$). In this panel, the clouds without fragmentation have almost the same magnetic field strength for $n_{\rm c} \lesssim 10^{16}\,{\rm cm}^{-3}$. For $n_{\rm c} \gtrsim 10^{16}\,{\rm cm}^{-3}$, the magnetic field continues to increase in the non-rotating cloud (Model 24), while they saturate a certain values in the rotating clouds (Models 25 and 26). On close inspection of the evolutions for $n_{\rm c} \gtrsim 10^{16}\,{\rm cm}^{-3}$, we can see that the growth rate of the magnetic field becomes small when the normalized angular velocity approaches $\Omega_{\rm c}/(4\pi G\rho_{\rm c})^{1/2} \simeq 0.2$. This is due to the fact that the collapse of the geometry changes from the spherical to the disk-like when the rotational energy becomes comparable to the gravitational energy [for detail, see Machida et al. 2005a]. Finally, the protostars have the magnetic fields of $B_{\rm c} = 0.51\,{\rm kG}$ (Model 24; $\omega = 0$), $0.48\,{\rm kG}$ (Model 25; $\omega = 0.001$), and $0.11\,{\rm kG}$ (Model 26; $\omega = 0.01$), respectively. In this way, the magnetic field strengths of the formed protostar are related to the initial cloud rotation. We can summarize that the protostar has a stronger magnetic field in more slowly rotating cloud.

The observation indicates that the molecular clouds have large amounts of magnetic energy (Crutcher 1999) and small amounts of rotational energy (Goodman et al. 1993; Caselli 2002). These clouds are classified into magnetic-force dominant cloud ($\Omega_0/B_0 < \Omega_{\rm cri}/B_{\rm cri} \equiv 0.39\, G^{1/2}\, c_s^{-1}$.) in the criterion of Machida et al. (2005a, 2006a). As shown in §4.1, the magnetic field converges to a certain value for the isothermal phase in magnetic-force dominant clouds. Thus, the magnetic field of protostar is determined almost only by the rotation energy of the initial cloud, when the degree of the resistivity (c_η) is fixed.

5. Discussion

5.1. Magnetic Flux Problem

The magnetic flux problem is important for the star formation process. Magnetic energy in an interstellar cloud is usually regarded to be comparable to the gravitational energy of the cloud, while the magnetic energy in a star is much smaller than the gravitational energy.

The molecular cloud can collapse when the following condition is realized

$$\Phi < \Phi_{\rm cri}, \tag{10}$$

where Φ means the magnetic flux and is defined as

$$\Phi = \int \boldsymbol{B} \cdot d\boldsymbol{S}, \tag{11}$$

$\Phi_{\rm cri}$ means the critical value of collapse and is defined as

$$\Phi_{\rm cri} = fG^{1/2}M, \tag{12}$$

where f and M stand for the dimensionless constant ($f \approx 8$; Mouschovias & Spitzer 1976; Tomisaka et al. 1998), and the mass of cloud or cloud core, respectively [5]. The observed magnetic fluxes of the molecular cloud cores (e.g., Crutcher 1999) are close to their critical value ($\Phi/\Phi_{\rm cri} \sim 1$), while those of protostar are much smaller than their critical value ($\Phi/\Phi_{\rm cri} \approx 10^{-5}$ – 10^{-3}; Johns-Krull et al. 2001). Thus, the magnetic flux should be largely removed from the cloud core during the star formation process. This is called "the magnetic flux problem" in the star formation.

The flux to ratio Φ/M around the center of the cloud decreases by two mechanisms in the collapsing cloud. One is the vertical collapse (Nakano 1983; Machida et al. 2005a), another is Ohmic dissipation (Nakano et al. 2002). When the gas infalls vertically along the magnetic field line (vertical collapse), the mass around the central region increases keeping the magnetic flux constant. Thus, the ratio of the magnetic flux to the critical mass, $\Phi/\Phi_{\rm cri}$ ($\propto \Phi/M$), decreases, because the denominator of $\Phi/\Phi_{\rm cri}$ increases, and the numerator keeps nearly constant. Nakano (1983) shows that, however, this vertical collapse mechanism is not sufficient to solve the magnetic flux problem, because the large amount of the gas is gathered from the wide range ($> 200\,{\rm kpc}$) to decrease this ratio from $\Phi/\Phi_{\rm cri} \simeq 1$ up to $\sim 10^{-5}$ – 10^{-3}. On the other hand, Nakano et al. (2002) shows that Ohmic dissipation process in the collapsing cloud is an effective mechanism to solve the magnetic flux problem in their analytical study. We numerically reconfirmed that Ohmic dissipation is more important process than the vertical collapse for removal (or decrease) of the magnetic flux in the collapsing cloud.

---

[5] In general, the values of Φ and $\Phi_{\rm cri}$ are used to measure the degree of the magnetic field strength of the isolated cloud core. In this paper, however, we use these values to measure the degree of the magnetic field strength inside the collapsing cloud core. We simply define Φ and $\Phi_{\rm cri}$ as a function of the magnetic field and mass in the local region inside the cloud core.

Figure 11*a* shows the distribution of the magnetic flux normalized by the critical mass ($\Phi/\Phi_{\rm cri}$) as a function of the cumulative mass from the center of the cloud at the initial state (broken line), and at the end of the calculation for Models 29 (solid line) and 30 (dotted line). In this panel, the mass (M; x-axis) is integrated every iso-density contour ($\rho_{\rm a}$) from the center that has the maximum density as

$$M(\rho > \rho_{\rm a}) = \int_{\rho>\rho_{\rm a}} \rho \, dV, \tag{13}$$

and the magnetic flux inside the corresponding region is also integrated as

$$\Phi(\rho > \rho_{\rm a}) = \int_{\rho>\rho_{\rm a}, z=0} \boldsymbol{B} \cdot d\boldsymbol{S}, \tag{14}$$

where $d\boldsymbol{S}$ is defined at $z = 0$ plane and parallel to the z-axis. This panel indicates that Models 29 and 30 has magnetically supercritical clouds ($\Phi/\Phi_{\rm cri} < 1$) as a whole ($M > 0.3\,M_\odot$), while the central regions ($M < 0.3\,M_\odot$) in these clouds are magnetically subcritical ($\Phi/\Phi_{\rm cri} < 1$) at the initial state. The ratio of $\Phi/\Phi_{\rm cri}$ increases with decreasing the mass. The initial density distribution near the center is almost constant as we adopt the Bonnor-Ebert density profile (Bonnor 1956; Ebert 1955), thus the mass of the cloud (i.e., $\Phi_{\rm cri}$) is proportional to R^3, $M \propto \Phi_{\rm cri} \propto R^3$. On the other hand, the magnetic flux is proportional to $\Phi \propto R^2$, because the uniform magnetic field is assumed at the initial state. Thus, the central region (i.e., small amount of the mass) has large $\Phi/\Phi_{\rm cri}$, since the ratio of magnetic flux to the critical mass is proportional to $\Phi/\Phi_{\rm cri} \propto R^{-1} \propto M^{-1/3}$ near the center. However, these clouds can collapse promptly, because a large amount of the mass ($\sim 99\%$ of the total mass) is a magnetically supercritical.

In our calculations, the protostars have the mass of $\sim 10^{-3}\,M_\odot$ at their formation epoch. Figure 11*a* shows that the magnetic flux to critical mass ratio within the mass of $M = 10^{-3}\,M_\odot$ (at $M = 10^{-3}\,M_\odot$ on the x-axis) decreases from $\Phi/\Phi_{\rm cri} = 6$ to $\Phi/\Phi_{\rm cri} \simeq 0.2$ in the ideal MHD model (Model 30). In Model 30, the ratio $\Phi/\Phi_{\rm cri}$ decreases due to the vertical collapse, because Ohmic dissipation is ignored ($c_\eta = 0$). This indicates that the magnetic flux is not removed sufficiently by the vertical collapse as shown in Nakano (1983). On the other hand, in Model 29 (the non-ideal MHD model), the ratio $\Phi/\Phi_{\rm cri}$ within $M = 10^{-3}\,M_\odot$ decreases from $\Phi/\Phi_{\rm cri} = 6$ to $\Phi/\Phi_{\rm cri} \simeq 10^{-3}$ (Fig. 11*a*). Thus, three or four orders of magnitude of the initial magnetic flux is removed from the core by Ohmic dissipation in Model 29. The solid line in Figure 11*a* shows that the ratio $\Phi/\Phi_{\rm cri}$ decreases from $\Phi/\Phi_{\rm cri} \simeq 0.1$ to $\Phi/\Phi_{\rm cri} \simeq 10^{-3}$ steeply between $10^{-2}\,M_\odot \lesssim M \lesssim 5 \times 10^{-3}\,M_\odot$. This drop indicates that the gas within $M < 10^{-2}\,M_\odot$ from the center of the cloud experiences Ohmic dissipation. The remainder of the cloud is expected to experience Ohmic dissipation as the collapse continues.

Figure 11*b* shows the evolution of $\Phi/\Phi_{\rm cri}$ for Models 29-32 against the central density. In this panel, the magnetic flux (Φ) and the mass (M) within the gas having the density of $\rho > 0.1\rho_{\rm c}$ are integrated at each timestep as

$$M(\rho > 0.1\rho_{\rm c}) = \int_{\rho>0.1\rho_{\rm c}} \rho \, dV, \tag{15}$$

$$\Phi(\rho > 0.1\rho_{\rm c}) = \int_{\rho>0.1\rho_{\rm c}} \boldsymbol{B} \cdot d\boldsymbol{S}. \tag{16}$$

The ratios $\Phi/\Phi_{\rm cri}$ in the ideal MHD models (Models 30 and 32) decrease slightly from the initial ($\Phi/\Phi_{\rm cri} \simeq 0.8$) to the protostar formation epoch ($\Phi/\Phi_{\rm cri} \simeq 0.2$). In contrast, the ratios $\Phi/\Phi_{\rm cri}$ in the non-ideal MHD models (Model 29 and 31) decrease significantly during $2 \times 10^{12}\,{\rm cm}^{-3} \lesssim n_{\rm c} \lesssim 6 \times 10^{15}\,{\rm cm}^{-3}$ by Ohmic dissipation, and reach $\Phi/\Phi_{\rm cri} \simeq 10^{-3}$ at the protostar formation epoch.

In the non-ideal MHD models, the formed protostars has a smaller ratios of $\Phi/\Phi_{\rm cri}$ in a more rapidly rotating cloud. After the magnetic dissipation ($n_{\rm c} \gtrsim 10^{16}\,{\rm cm}^{-3}$), the evolutions of the ratio $\Phi/\Phi_{\rm cri}$ are different in the non-ideal Models 29 and 31 (Fig. 11b). For this phase ($n_{\rm c} \gtrsim 10^{16}\,{\rm cm}^{-3}$), this ratio keeps almost the constant value ($\Phi/\Phi_{\rm cri} \simeq 5 \times 10^{-4}$) in Model 31 (rapidly rotating cloud), while it continues to increase in Model 29 (slowly rotating cloud). At the protostar formation epoch, the protostars have $\Phi/\Phi_{\rm cri} = 2 \times 10^{-3}$ (Model 29), and $\Phi/\Phi_{\rm cri} = 4 \times 10^{-4}$ (Model 31), respectively. This difference is caused by the rotation rate of the initial cloud. In Model 31, the cloud collapses vertically (i.e., the vertical collapse), and the growth rate of the magnetic field is small because of the rapid rotation for $n_{\rm c} \gtrsim 10^{16}\,{\rm cm}^{-3}$. On the other hand, in Model 29, the cloud collapses spherically (i.e., the spherical collapse) and the growth rate of the magnetic field is large for $n_{\rm c} \gtrsim 10^{16}\,{\rm cm}^{-3}$, because both the Lorentz and centrifugal forces are weak. After the magnetic dissipation ($n_{\rm c} \gtrsim 10^{16}$), since the Lorentz force become weak, the geometry of the collapse is determined by the cloud rotation. The cloud collapses spherically to form the protostar with large magnetic flux in an initially slowly rotating cloud, while the cloud collapses along the rotation axis to form the protostar with a small magnetic flux in a rapidly rotating cloud.

As a results, the protostars have $\Phi/\Phi_{\rm cri} \simeq 10^{-4}$ to 10^{-3} at their formation epoch, which are comparable to the observation. However, since we stopped our calculation at $M \sim 10^{-3}\,M_\odot$, further calculation is needed to predict the correct value of the magnetic flux in the protostar of $M \sim 1\,M_\odot$.

5.2. Angular Momentum Problem

The angular momentum problem is important for the star formation process, as well as the magnetic flux problem. The molecular cloud cores have the specific angular momenta on the order of $j_{\rm cloud} \approx 10^{21}{\rm cm^2\,s^{-1}}$ (Goodman et al. 1993; Caselli 2002), while protostars have the specific angular momenta on the order of $j_{\rm protostar} \approx 10^{16}{\rm cm^2\,s^{-1}}$. Thus, the specific angular momentum of protostar is $\sim 10^{-5}$ times smaller than that of the molecular cloud core. For this reason, the angular momentum of the initial cloud should be removed from the core as well as the magnetic flux of the cloud. Tomisaka (2000, 2002) calculated the cloud evolutions from the molecular cloud to the protostar formation paying attention to the evolution of the angular momentum in his two-dimensional nested grid simulations. He has shown that the angular momentum of the initial cloud is sufficiently removed by the magnetic braking and outflow in the collapsing cloud, and the formed protostar has the specific angular momentum comparable to the observed value. However, he used the ideal MHD approximation, thus he may have overestimated the magnetic effect (i.e., magnetic braking and outflow). In this section, we discuss the evolution of the angular momentum in the non-ideal MHD regime.

Figure 11*c* shows the distributions of the specific angular momentum against the cumulative mass at the initial state (thick broken line), and the end of the calculation for Models 29 (solid line), 30 (thin broken line) , and 33 (dash-dotted lines). In this figure, the specific angular momentum are integrated up to every iso-density surface ($\rho_{\rm a}$) from the center as

$$j(\rho > \rho_{\rm a}) = \frac{1}{M(\rho > \rho_{\rm a})} \int_{\rho > \rho_{\rm a}} \rho\, \varpi \cdot v_\phi \, dV, \tag{17}$$

where $M(\rho > \rho_{\rm a})$ and ϖ mean the mass within $\rho > \rho_{\rm a}$ [see Equation (15)] and the radius in the cylindrical coordinate, respectively. As shown by the thick dashed line in Figure 11*c*, the specific angular momentum at the initial state is proportional to $j_{\rm cloud} \propto R^2$ near the center of the cloud, because we started with the rigid rotation and the Bonnor-Ebert density profile that has almost constant density at the center.

In Figure 11*c*, a dash-dotted line shows the specific angular momentum at the end of the calculation ($j_{\rm protostar}$) for Model 33. In Model 33, the specific angular momentum is not removed by the magnetic effects (the magnetic braking, outflow and jet), because the cloud is unmagnetized. Thus, the distribution of the specific angular momentum at the end of the calculation for Model 33 is almost the same as that of the initial state for $M > 10^{-2}\,M_\odot$. This indicates that the angular momentum is almost conserved outside the protostar ($M > 10^{-2}\,M_\odot$). For $M < 10^{-2}\,M_\odot$, the specific angular momentum at the end of the calculation is slightly smaller than that at the initial state, which is caused by the angular momentum transfer by the non-axisymmetric pattern. In this model, after a thin

disk is formed, the disk is transformed into the bar, because the bar mode instability (e.g., Durisen et al. 1986) is caused by the rapid rotation. The specific angular momentum begins to decrease around the center of the cloud as the non-axisymmetric pattern grows. We can observe the fragmentation in this unmagnetized model for further calculation as also shown by Banerjee & Pudritz (2006). As discussed in Machida et al. (2005b), fragmentation plays an important role in the angular momentum evolution, because the angular momentum is redistributed into the orbital and spin angular momentum of each fragment. We will discuss the fragmentation and redistribution of the angular momentum in subsequent papers.

The specific angular momenta of the magnetized clouds at the end of the calculation are plotted by the solid (the non-ideal MHD model; Model 29) and thin broken line (the ideal MHD model; Model 30) in Figure 11*c*. Both in Models 29 and 30, the specific angular momenta at the end of the calculation are smaller than those at the initial state. In these models, the specific angular momentum decreases by the vertical collapse, magnetic braking, outflow, and jet. When the initial cloud is magnetized strongly (or rotates rapidly), the cloud collapses vertically along the magnetic field line (i.e., the vertical collapse). The gas having smaller amount of the specific angular momentum preferentially falls onto the central region, and thus the central region gains specific angular momentum in the vertical collapse regime. Note that the vertical collapse does not transfer the angular momentum, because this mechanism changes only the location of each fluid element the gas keeping its specific angular momentum. For higher density ($n_{\rm c} \gtrsim 10^{11}\,{\rm cm}^{-3}$), the magnetic field lines are strongly twisted, and outflow and jet appear. The angular momentum is effectively transferred by the outflow and jet as already shown by Tomisaka (2000, 2002). The simple magnetic braking is also important for the angular momentum transfer. In principle, however, we cannot distinguish the reduction of angular momentum due to magnetic braking from that due to outflow and jet, because the outflow and jet are consequences of magnetic braking process.

Figure 11*d* shows the evolution of specific angular momentum j in the inner region for Models 29, 30, and 33 as a function of the central density. The angular momentum is integrated within $\rho > 0.1\rho_{\rm c}$ at each timestep and averaged as

$$j(\rho > 0.1\rho_{\rm c}) = \frac{1}{M(\rho > 0.1\rho_{\rm c})} \int_{\rho > 0.1\rho_{\rm c}} \rho\, \varpi \cdot v_\phi \, dV, \tag{18}$$

where $M(\rho > 0.1\rho_{\rm c})$ is the mass within $\rho > 0.1\rho_{\rm c}$. In this panel, the specific angular momenta in the magnetized clouds (Models 29, and 30) are smaller than that in unmagnetized cloud (Model 33) for $n_c \gtrsim 10^6\,{\rm cm}^{-3}$. The difference of the specific angular momentum for the isothermal phase ($n_{\rm c} \lesssim 10^{11}\,{\rm cm}^{-3}$) is caused by the magnetic braking and vertical collapse, because no outflow appears in this phase. In the magnetized clouds (Models 29, and 30), the specific angular momentum in Model 30 (ideal MHD model) becomes smaller than that in

Model 29 (non-ideal MHD model) for $n_c \gtrsim 10^{15}\,\mathrm{cm}^{-3}$, because the magnetic braking becomes less effective due to the magnetic dissipation during $2 \times 10^{12}\,\mathrm{cm}^{-3} \lesssim n_c \lesssim 6 \times 10^{15}\,\mathrm{cm}^{-3}$.

At the protostar formation epoch ($n_c = 10^{21}\,\mathrm{cm}^{-3}$), the protostars have the specific angular momenta of $j_{\mathrm{protostar}} = 8 \times 10^{16}\,\mathrm{cm}^2\,\mathrm{s}^{-1}$ (Model 31), $1.5 \times 10^{15}\,\mathrm{cm}^2\,\mathrm{s}^{-1}$ (Model 29), and $2 \times 10^{14}\,\mathrm{cm}^2\,\mathrm{s}^{-1}$ (Model 30), respectively. Observations indicate that classical T Tauri stars have the specific angular momenta on the order of the $j_{\mathrm{obs}} \sim 10^{16}\mathrm{cm}^2\,\mathrm{s}^{-1}$ (Bouvier et al. 1993; Herbst et al. 2006). At the end of our calculation, the formed protostars have only the mass of $\sim 10^{-3}\,M_\odot$. Since the spatial distribution of specific angular momentum is proportional to $j \propto \varpi^2$ in the case of rigid rotation, the region inside $M < 10^{-3}\,M_\odot$ of T Tauri stars has the average specific angular momentum of $\sim 10^{14}\mathrm{cm}^2\,\mathrm{s}^{-1}$. Thus, specific angular momenta in the non-ideal MHD models (Model 29) are about one-order-magnitude larger than those in observed protostars. In this paper, we are discussing the angular momentum evolution in the early star formation phase ($M_{\mathrm{protostar}} < 10^{-2} - 10^{-3}\,M_\odot$). In the later accretion phase, however, the angular momentum will be transferred by the star-disk interaction, stellar wind, and jet. To actually solve the angular momentum problem, we need to calculate the evolution in much later phase.

In this paper, to focus on the formation of single stars, we investigate the evolution of slowly rotating clouds. As shown in Cha & Whitworth (2003), Matsumoto & Hanawa (2003), and Machida et al. (2005b), fragmentation occurs in the collapsing cloud core, and the binary of multiple stars are formed in the initially rapidly rotating clouds. When the binary or multiple stars are formed, the angular momentum is redistributed into the orbital and spin angular momenta of each star (Machida et al. 2005b). Thus, the binary or multiple star formation process is also important for the angular momentum problem. We will investigate the evolution in the initially rapidly rotating clouds in subsequent papers.

5.3. Comparison with Observations

In our calculation, the formed protostars have the magnetic field of $B_{\mathrm{protostar}} = 0.16\,\mathrm{kG}$ (Model 16) - 1.53 kG (Model 32) in models with $\eta = 1$ (non-ideal MHD Models 16, 22, 24, 25, 26, 27, and 28). On the other hand, surface magnetic field of order of 1-3 kG have been derived from Zeeman broadening measurement of CTTS photospheric lines (Johns-Krull et al. 1999a,b, 2001; Guenther et al. 1999; Bouvier et al. 2005). Thus, the magnetic fields derived from our calculation are well consistent with the observations. On the other hand, the rotation periods of protostars in our calculation are slightly shorter than the observations. The formed protostars have the rotation period of $P = 0.15$ days (Model 26) to 1.53 days (Model 32) in model with $c_\eta = 1$, while the observed protostars have the rotation period of

$P = 1 - 10$ days (Herbst et al. 2006).

Since our calculation shows only the early star formation phase, in which the protostars have the mass of $\simeq 10^{-3} - 10^{-2}\,M_\odot$. Thus, the magnetic field strength and angular momentum of protostar may change in subsequent gas accretion phase. The magnetic field may be amplified by the magneto-rotational instability (Balbus & Hawley 1991) and by the shearing motion between the star and the ambient medium. The angular momentum of protostar may increase by the accretion of gas with larger angular momentum, and decrease by the jet and star-disk interaction (e.g., Matt & Pudritz 2005a,b). We should calculate the cloud evolution until later accretion phase to understand the magnetic field and angular momentum of protostar more precisely. However, our results indicate that the protostar at its formation epoch already have almost the same orders of the magnitude of the magnetic field strength and rotation period as the observation. Thus, the magnetic field and angular momentum of the observed protostar may be mainly made for the early star formation phase before the main accretion phase.

We have greatly benefited from discussion with T. Nakano, and K. Saigo. We also thank T. Hanawa for contribution to the nested grid code. Numerical calculations were carried out with a Fujitsu VPP5000 at the Astronomical Data Analysis Center, the National Astronomical Observatory of Japan. This work is supported by the Grant-in-Aid for the 21st Century COE "Center for Diversity and Universality in Physics" from the Ministry of Education, Culture, Sports, Science and Technology (MEXT) of Japan, and partially supported by the Grants-in-Aid from MEXT (15740118, 16077202, 18740113,18740104).

REFERENCES

Balbus, S. A., & Hawley, J. F. 1991, ApJ, 376, 214

Banerjee, R., & Pudritz, R. E. 2006, ApJ, 641, 949

Basu S., & Moushovias T. Ch., 1994, ApJ, 432, 720

Bate M., 1998, ApJ, 508, L95

Bonnor, W. B. 1956, MNRAS, 116, 351

Bouvier, J., Cabrit, C., Fernández, M., Martin, E. L., & Matthews, J. 1993, A&A, 272, 176

Bouvier, J., Alencar, S. H. P., Harries, T. J., Johns-Krull, C. M., & Romanova, M. M., 2005, in Protostars and Planets V, ed. B. Reipurth, D. Jewitt, & K. Keil (Tucson: Univ. Arizona Press), in press

Bacciotti, F., Ray, T. P., Mundt, R., Eislöffel, J., & Solf, J. 2002, ApJ, 576, 222

Belloche A., Andé P., Despois D., Blinder S. 2002, A&A, 393, 927

Blandford, R. D., & Payne, D. G. 1982, MNRAS, 199, 883

Bouvier, J., Alencar, S. H. P., Harries, T. J., Johns-Krull, C. M., & Romanova, M. M. 2006, in Protostars and Planets V, ed. B. Reipurth, D. Jewitt, & K. Keil (Tucson: Univ. Arizona Press), in press (astro-ph/0603498)

Caselli, P., Benson, P. J., Myers, P. C., & Tafalla, M. 2002, ApJ, 572, 238

Cha, S.-H., & Whitworth, A. P. 2003, MNRAS, 340,

Crutcher R. M. 1999, ApJ, 520, 706

Dedner A., Kemm F., Kröner D., Munz C.-D., Schnitzer T., Wesenberg M., 2002, J. Comp. Phys., 175, 645

Durisen R.H., Gingold R.A., Tohline J.E., & Boss A.P., 1986, ApJ, 305, 281

Ebert, R. 1955, Z. Astrophys., 37, 222

Girart, J. M., Rao, R., & Marrone, D. P., 2006, Science, 313, 812

Goodman, A. A., Benson, P. J., Fuller, G. A., & Myers, P. C. 1993, ApJ, 406, 528

Guenther, E. W., Lehmann, H., Emerson, J. P., & Staude, J. 1999, A&A, 341, 768

Herbst, W., Eisloeffel, J., Mundt, R., & Scholz, A. 2006, in Protostars and Planets V, ed. B. Reipurth, D. Jewitt, & K. Keil (Tucson: Univ. Arizona Press), in press (astro-ph/0603673)

Hosking J. G., & Whitworth A. P., 2004 MNRAS, 347, 3

Johns-Krull, C. M., Valenti, J. A., Hatzes, A. P., & Kanaan, A. 1999a, ApJ, 510, L41

Johns-Krull, C. M., Valenti, J. A., & Koresko, C. 1999b, ApJ, 516, 900

Johns-Krull, C. M., Valenti, J. A., Piskunov, N. E., Saar, S. H., & Hatzes, A. P. 2001, in ASP Conf. Ser. 248, Magnetic Fields Across the Hertzsprung-Russell Diagram, ed. G. Mathys, S. K. Solanki, & D. T. Wickramasinghe (San Francisco: ASP), 527

Larson, R. B., 1969, MNRAS, 145, 271.

Machida, M. N., Tomisaka, K., & Matsumoto, T. 2004, MNRAS, 348, L1

Machida, M. N., Matsumoto, T., Tomisaka, K., & Hanawa, T. 2005, MNRAS, 362, 369

Machida, M. N., Matsumoto, T., Hanawa, T., & Tomisaka, K. 2005, MNRAS, 362, 382

Machida, M. N., Matsumoto, T., Hanawa, T., & Tomisaka, K. 2006, ApJ, 645, 1227

Machida, M. N., Matsumoto, T., & Inutsuka, S., 2006, ApJ, accepted

Masunaga, H., & Inutsuka, S., 2000, ApJ, 531, 350

Masunaga, H., Miyama, S. M., & Inutsuka, S., 1998, ApJ, 495, 346

Matsumoto, T., Hanawa, T., & Nakamura, F. 1997, ApJ, 478, 569

Matsumoto, T., & Hanawa, T. 2003, ApJ, 595, 913

Matsumoto T., & Tomisaka K., 2004, ApJ, 616, 266

Matt, S., & Pudritz, R. 2005a, ApJ, 632, L135

Matt, S., & Pudritz, R., 2005b MNRAS, 356, 167

Mouschovias, T. Ch., & Spitzer, L. 1976, ApJ, 210, 326

Nakano, T., 1983, PASJ, 35, 87

Nakano, T., 1984, Fundam. Cosm. Phys., 9, 139

Nakano, T., Nishi, R., & Umebayashi, T. 2002, ApJ, 573, 199

Saigo, K., & Tomisaka, K., 2006, ApJ, 645, 381

Truelove J, K., Klein R. I., McKee C. F., Holliman J. H., Howell L. H., & Greenough J. A., 1997, ApJ, 489, L179

Tomisaka, K., Ikeuchi, S., & Nakamura, T. 1988, ApJ, 335, 239

Tomisaka K. 1998, ApJ, 502, L163

—, 2000, ApJ, 528, L41

—, 2002, ApJ, 575, 306

Whitehouse S. C., & Bate M. R., 2006, astro-ph/0511671

Winkler, K.-H. A., & Newman, M. J. 1980a, ApJ, 236, 201

—, 1980b, ApJ, 236, 201

Ziegler, U. 2005, A&A, 435, 385

Table 1: Model parameters and calculation results

Model	α	ω	c_η	f	B_0 [μG]	Ω_0 [s^{-1}]	M[$M_\odot$]	α_0	β_0	γ_0	$B_{\rm f}$ (kG)	P (day)
1	5	0	0	1.4	34	0	6.3	0.6	0	5.8	89.7	∞
2	0.5	0	0	1.4	11	0	6.3	0.6	0	0.58	123	∞
3	0.1	0	0	1.4	5.0	0	6.3	0.6	0	0.12	106	∞
4	0.05	0	0	1.4	3.5	0	6.3	0.6	0	5.8×10^{-2}	102	∞
5	0.01	0	0	1.4	1.6	0	6.3	0.6	0	1.2×10^{-2}	92.5	∞
6	10^{-3}	0	0	1.4	0.5	0	6.3	0.6	0	1.2×10^{-3}	88.9	∞
7	0.01	10^{-3}	0	1.4	1.6	2.1×10^{-16}	6.3	0.6	3.3×10^{-6}	1.2×10^{-2}	95.9	46.8
8	0.01	0.01	0	1.4	1.6	2.1×10^{-15}	6.3	0.6	3.3×10^{-4}	1.2×10^{-2}	67.3	5.68
9	0.01	0.05	0	1.4	1.6	1.1×10^{-14}	6.3	0.6	8.2×10^{-3}	1.2×10^{-2}	46.2	4.30
10	0.01	0.1	0	1.4	1.6	2.1×10^{-14}	6.3	0.6	3.3×10^{-2}	1.2×10^{-2}	43.7	2.47
11	0.01	0.15	0	1.4	1.6	3.1×10^{-14}	6.3	0.6	7.4×10^{-2}	1.2×10^{-2}	—	—
12	0.01	0.01	0	1.2	1.4	2.0×10^{-15}	5.4	0.7	3.3×10^{-4}	1.2×10^{-2}	42.7	4.79
13	0.01	0.01	10^{-3}	1.2	1.4	2.0×10^{-15}	5.4	0.7	3.3×10^{-4}	1.2×10^{-2}	2.74	3.99
14	0.01	0.01	0.01	1.2	1.4	2.0×10^{-15}	5.4	0.7	3.3×10^{-4}	1.2×10^{-2}	0.93	3.89
15	0.01	0.01	0.1	1.2	1.4	2.0×10^{-15}	5.4	0.7	3.3×10^{-4}	1.2×10^{-2}	0.64	3.77
16	0.01	0.01	1	1.2	1.4	2.0×10^{-15}	5.4	0.7	3.3×10^{-4}	1.2×10^{-2}	0.11	3.68
17	0.01	0.01	10	1.2	1.4	2.0×10^{-15}	5.4	0.7	3.3×10^{-4}	1.2×10^{-2}	—	—
18	0.01	10^{-4}	0	1.2	1.4	2.0×10^{-17}	5.4	0.7	3.3×10^{-8}	1.3×10^{-2}	60.9	271.1
19	0.01	10^{-4}	10^{-3}	1.2	1.4	2.0×10^{-17}	5.4	0.7	3.3×10^{-8}	1.3×10^{-2}	41.7	81.2
20	0.01	10^{-4}	0.01	1.2	1.4	2.0×10^{-17}	5.4	0.7	3.3×10^{-8}	1.3×10^{-2}	13.2	72.6
21	0.01	10^{-4}	0.1	1.2	1.4	2.0×10^{-17}	5.4	0.7	3.3×10^{-8}	1.3×10^{-2}	2.81	102
22	0.01	10^{-4}	1	1.2	1.4	2.0×10^{-17}	5.4	0.7	3.3×10^{-8}	1.3×10^{-2}	0.68	109
23	0.01	10^{-4}	10	1.2	1.4	2.0×10^{-17}	5.4	0.7	3.3×10^{-8}	1.3×10^{-2}	0.32	72.9
24	0.01	0	1	1.2	1.4	0	5.4	0.7	0	1.3×10^{-2}	0.51	∞
25	0.01	0.001	1	1.2	1.4	2.0×10^{-16}	5.4	0.7	3.3×10^{-6}	1.3×10^{-2}	0.48	11.1
26	0.01	0.01	1	1.2	1.4	2.0×10^{-15}	5.4	0.7	3.3×10^{-4}	1.3×10^{-2}	0.11	4.21
27	0.01	0.03	1	1.2	1.4	5.9×10^{-15}	5.4	0.7	3.0×10^{-3}	1.3×10^{-2}	—	—
28	0.01	0.1	1	1.2	1.4	2.0×10^{-14}	5.4	0.7	3.3×10^{-2}	1.3×10^{-2}	—	—
29	1	0.01	1	1.4	16	2.1×10^{-15}	6.3	0.6	3.3×10^{-4}	1.2	0.89	5.56
30	1	0.01	0	1.4	16	2.1×10^{-15}	6.3	0.6	3.3×10^{-4}	1.2	36.1	59.9
31	1	0.05	1	1.4	16	1.3×10^{-14}	6.3	0.6	3.3×10^{-4}	1.2	0.30	5.38
32	1	0.05	0	1.4	16	1.3×10^{-14}	6.3	0.6	3.3×10^{-4}	1.2	28.4	12.0
33	0	0.01	—	1.4	0	2.1×10^{-15}	6.3	0.6	3.3×10^{-4}	1.2	—	4.86

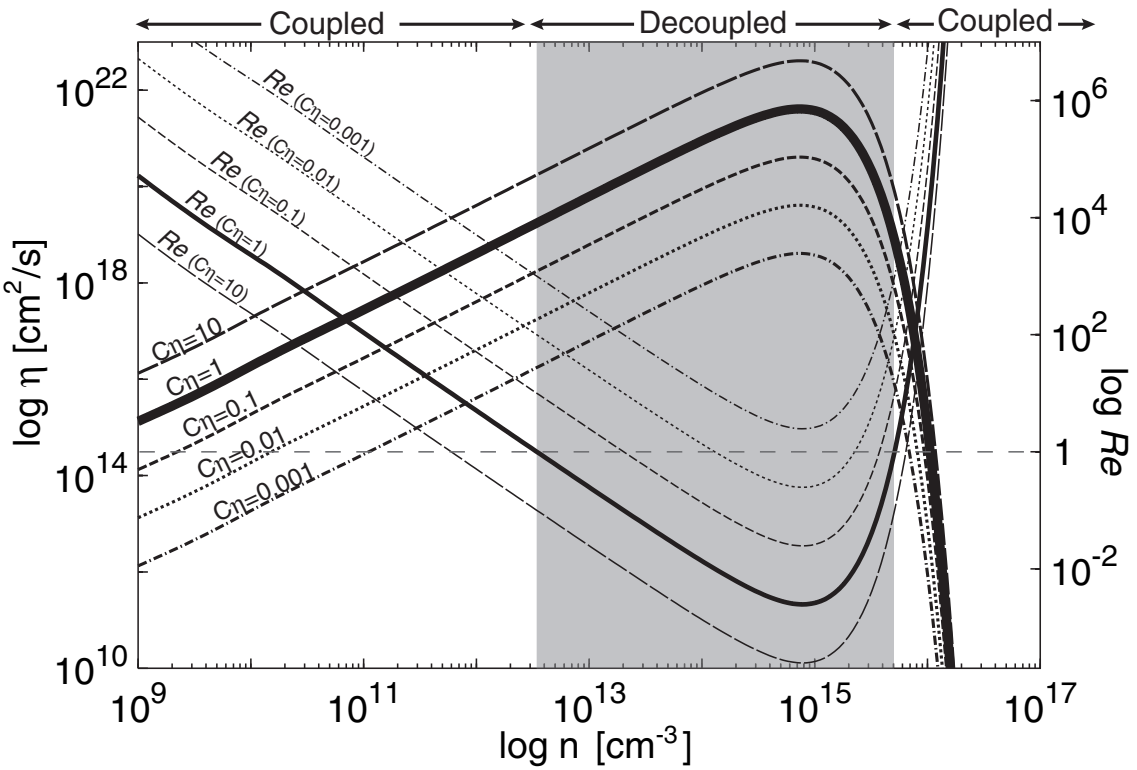

Fig. 1.— Resistivity (η; left axis) and magnetic Reynolds number (Re; right axis) as a function of the number density. Resistivity estimated by Nakano et al. (2002) is plotted by a thick solid line ($c_\eta = 1$), and corresponding magnetic Reynolds number by a thin solid line. The magnetic Reynolds number is analytically acquired by using free-fall velocity (v_f) and Jeans length (λ_j) estimated by given density and resistivity as $Re \equiv v_\mathrm{f}\lambda_\mathrm{j}\eta^{-1}$. Resistivities multiplied by factors 0.001 ($c_\eta = 0.001$), 0.01 ($c_\eta = 0.01$), 0.1 ($c_\eta = 0.1$), and 10 ($c_\eta = 10$), and corresponding magnetic Reynolds numbers are also plotted. The magnetic field well couple with the gas in "coupled" region, while the magnetic field decouples from the gas in "decoupled" region. Below vertical broken line $Re = 0$, Ohmic dissipation becomes effective. Thus, in shadowed region ($3 \times 10^{12} \lesssim n_\mathrm{c} \lesssim 5 \times 10^{15}\,\mathrm{cm}^{-3}$), the magnetic field is effectively dissipated by Ohmic dissipation, when $c_\eta = 1$ is adopted.

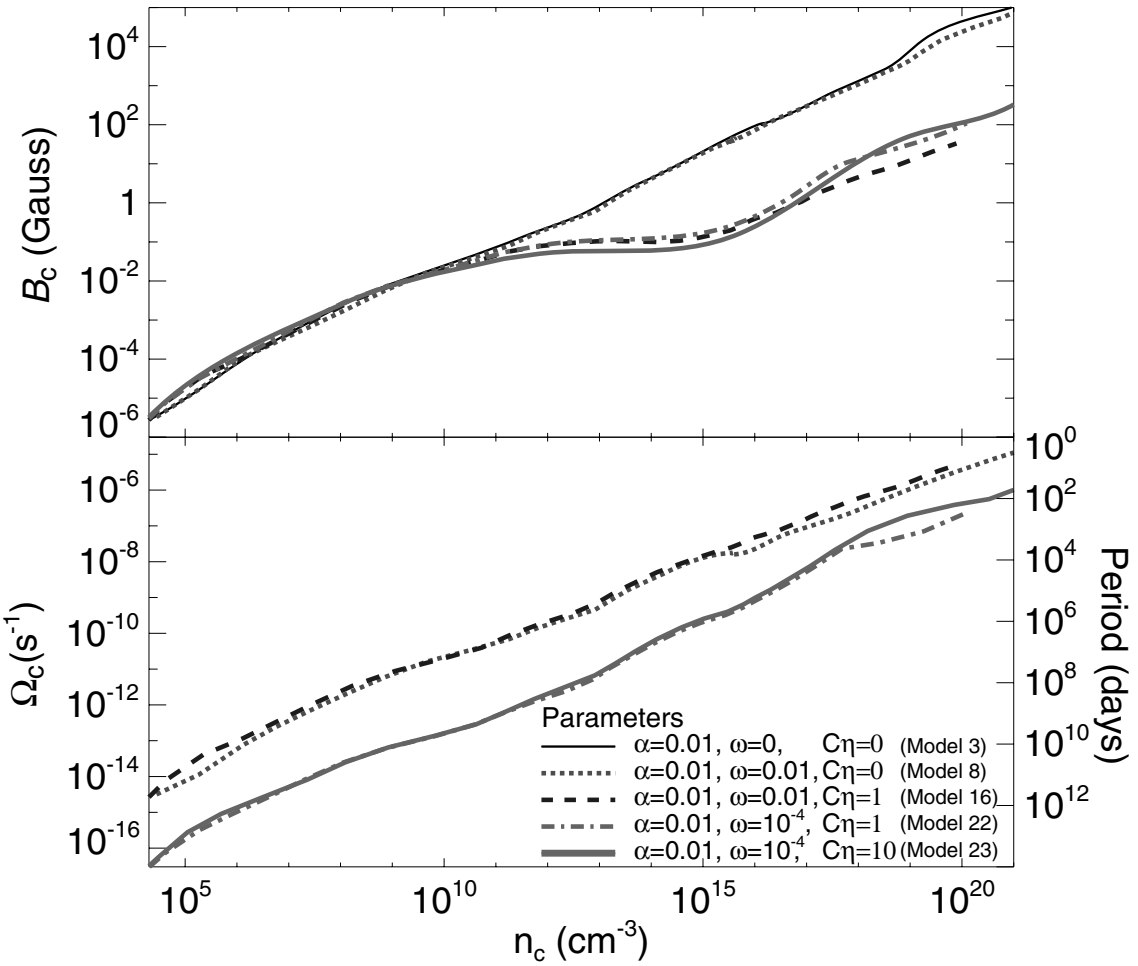

Fig. 2.— The evolution of central magnetic field (B_c; upper panel) and angular velocity (Ω_c; lower panel) against the number density at the center of the cloud for Models 3, 8, 16, 22, and 23. The rotation periods ($P = 2\pi/\Omega_c$) are also plotted on right axis of lower panel.

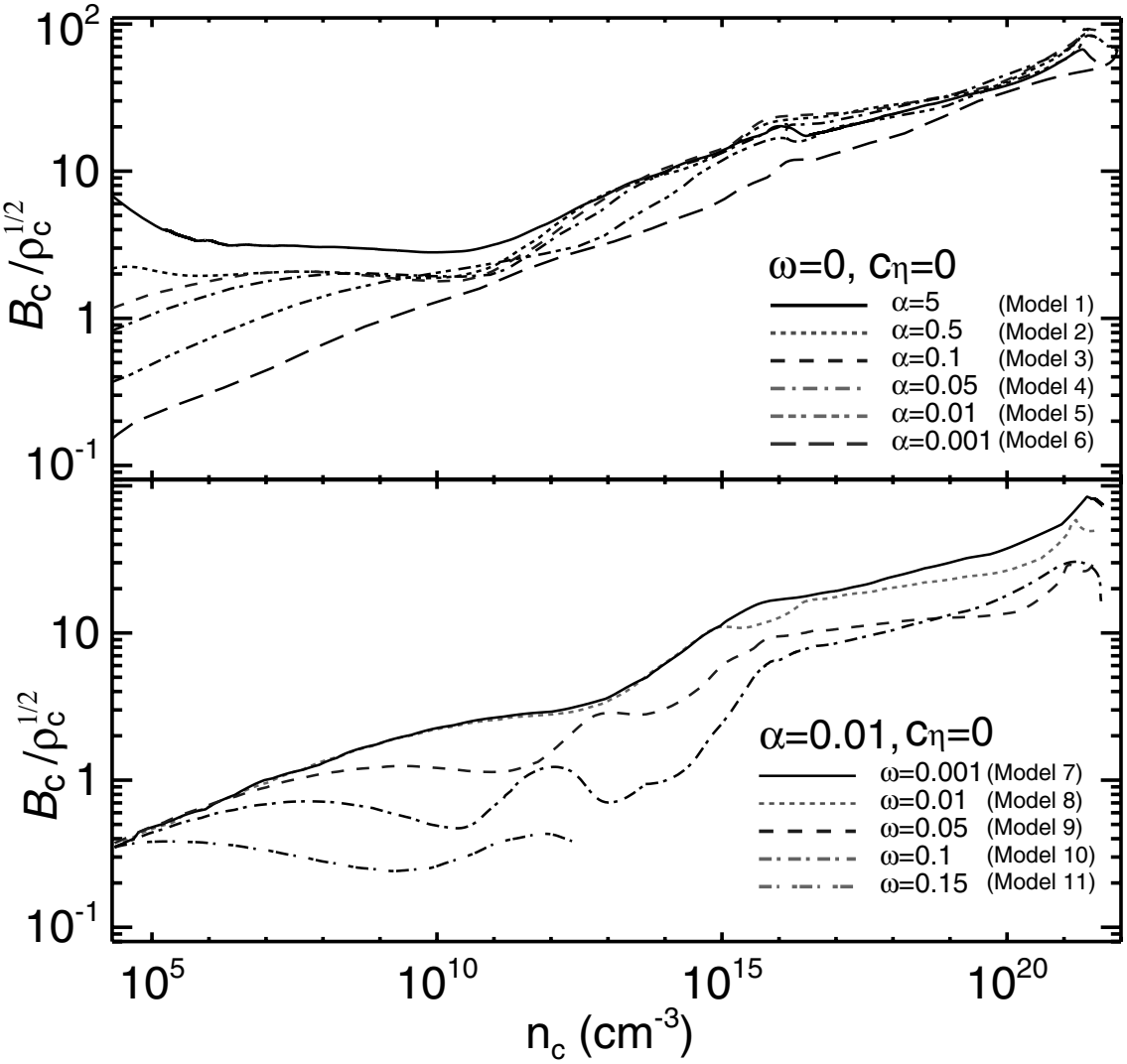

Fig. 3.— The magnetic fields (B_c) normalize by a square root of the densities ($\rho_c^{1/2}$) are plotted against the number density at the center of the cloud for Models 1-6 (upper panel), and for Models 7-11 (lower panel).

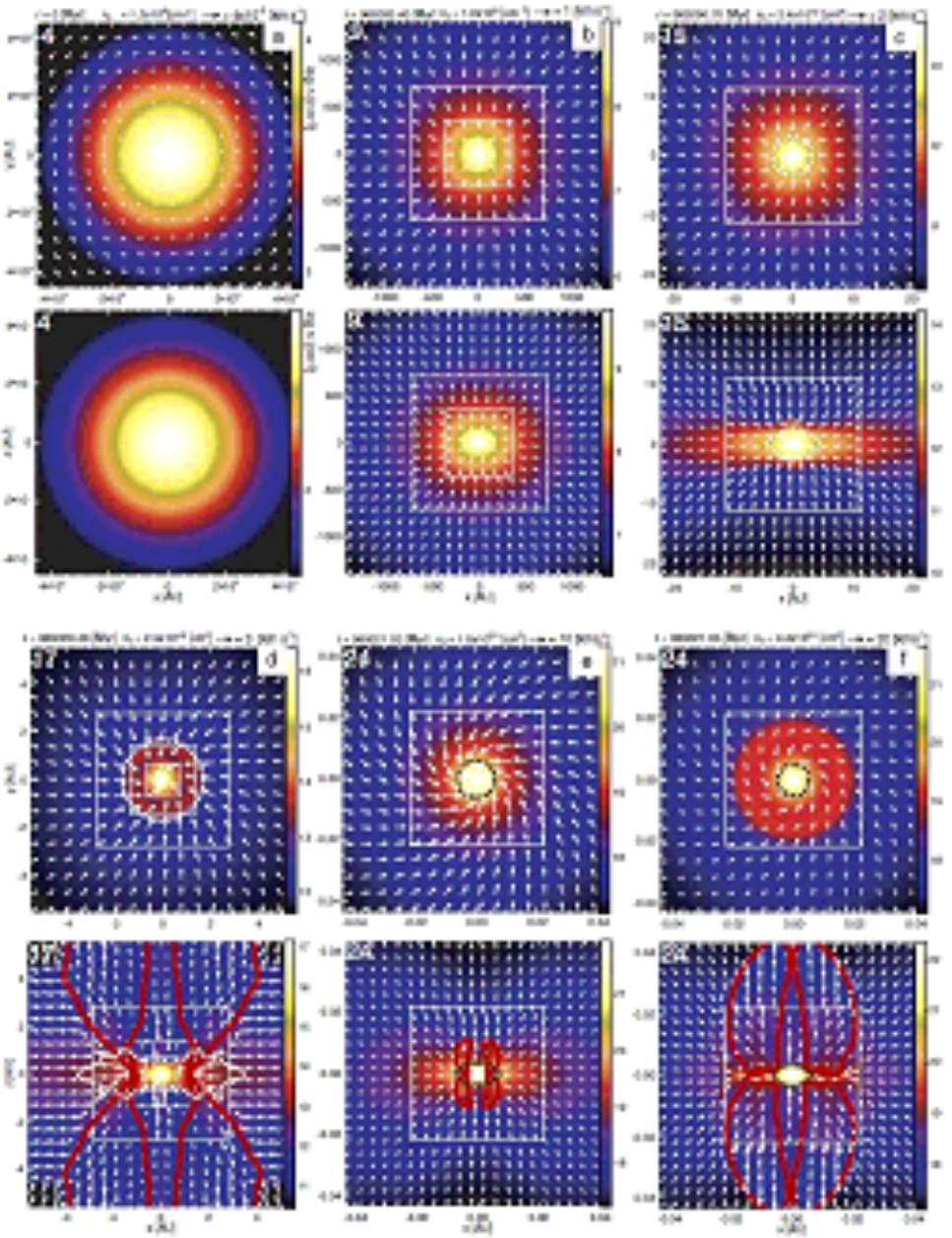

Fig. 4.— The density (color-scale) and velocity distribution (arrows) on the cross-section in the $z = 0$ plane (upper panels) and in the $y = 0$ plane (lower panels) for Model 12 [(α, ω, c_η) $= (0.01, 0.01, 0)$]. Panels (a) through (f) are snapshots at the stages of (a) $n_c = 1.2\times10^4\,\mathrm{cm}^{-3}$ ($l = 4$; initial state), (b) $1.0 \times 10^9\,\mathrm{cm}^{-3}$ ($l = 9 - 11$; isothermal phase), (c) $3.4 \times 10^{13}\,\mathrm{cm}^{-3}$ ($l = 15, 16$; adiabatic phase), (d) $2.5 \times 10^{16}\,\mathrm{cm}^{-3}$ ($l = 17 - 20$; second collapse phase), (e) $1.8\times10^{21}\,\mathrm{cm}^{-3}$($l = 24, 25$; protostellar phase), and (f) $4.4\times10^{21}\,\mathrm{cm}^{-3}$($l = 24, 25$; calculation end), where l denotes the level of subgrid. Dotted lines indicate the first core (white) and second core (black) that are surrounded by the shock surfaces. Red thick lines indicate the border between the infalling and outflowing gas ($v_{\rm out} \geq 0$ km s^{-1}). The level of the subgrid is shown in the upper left corner of each upper panel. The elapsed time (t), density at the center ($n_{\rm c}$), and arrow scale are denoted in each panel.

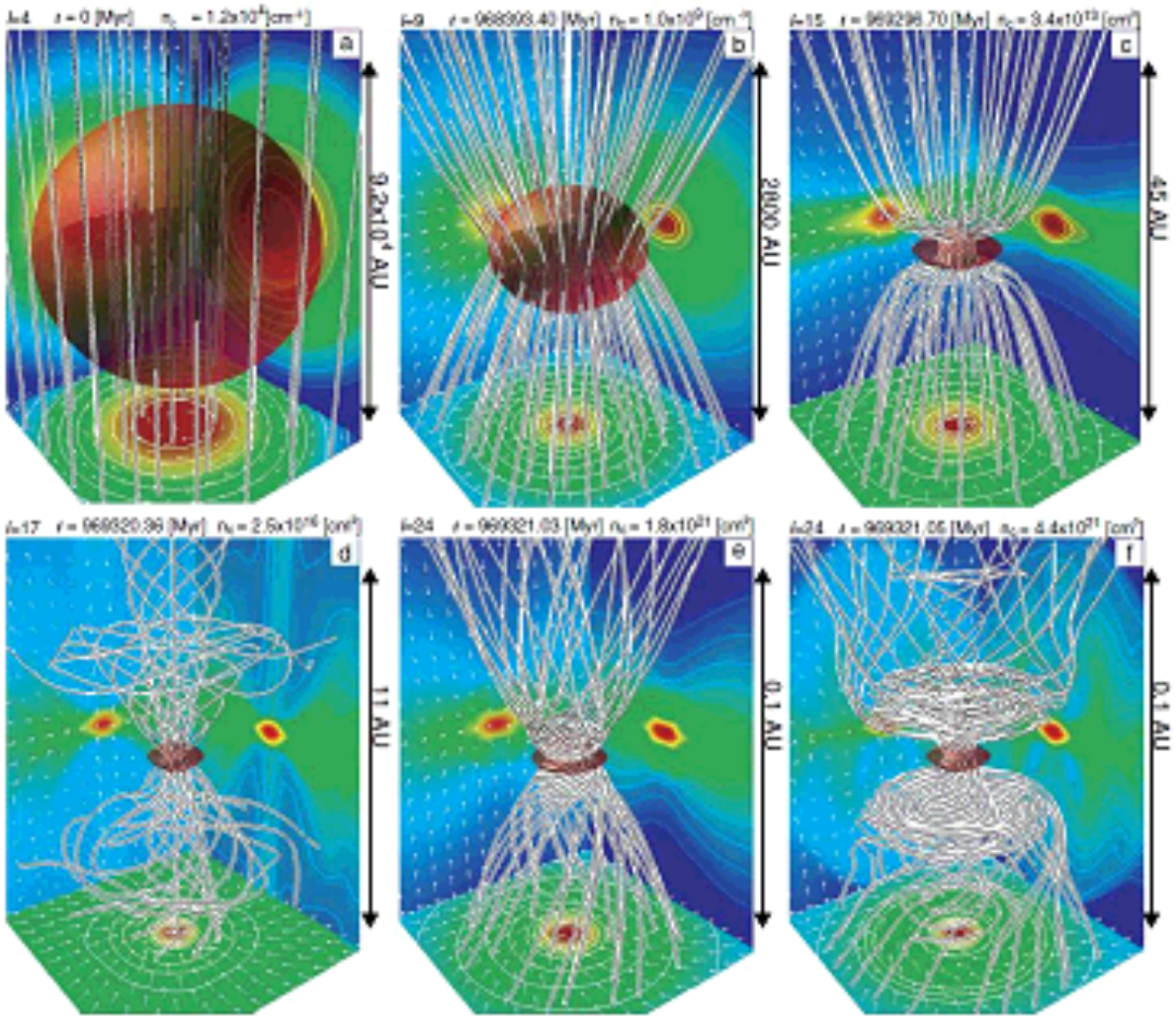

Fig. 5.— Birs'eys view of Fig. 4. Panels (a)-(f) are the same scale and same epoch as panels (a)-(f) of Fig. 4. The structure of high-density region ($\rho > 0.1\rho_c$; red iso-density surface), and magnetic field lines (black-and-white streamlines) are plotted in each panel. The density contours (false color and contour lines), velocity vectors (arrows) on the cross-section in the $x = 0$, $y = 0$, and z =0 plane are, respectively, projected in each wall surface. The grid level(l), elapsed time (t), density at the center (n_c), and grid scale are denoted in each panel.

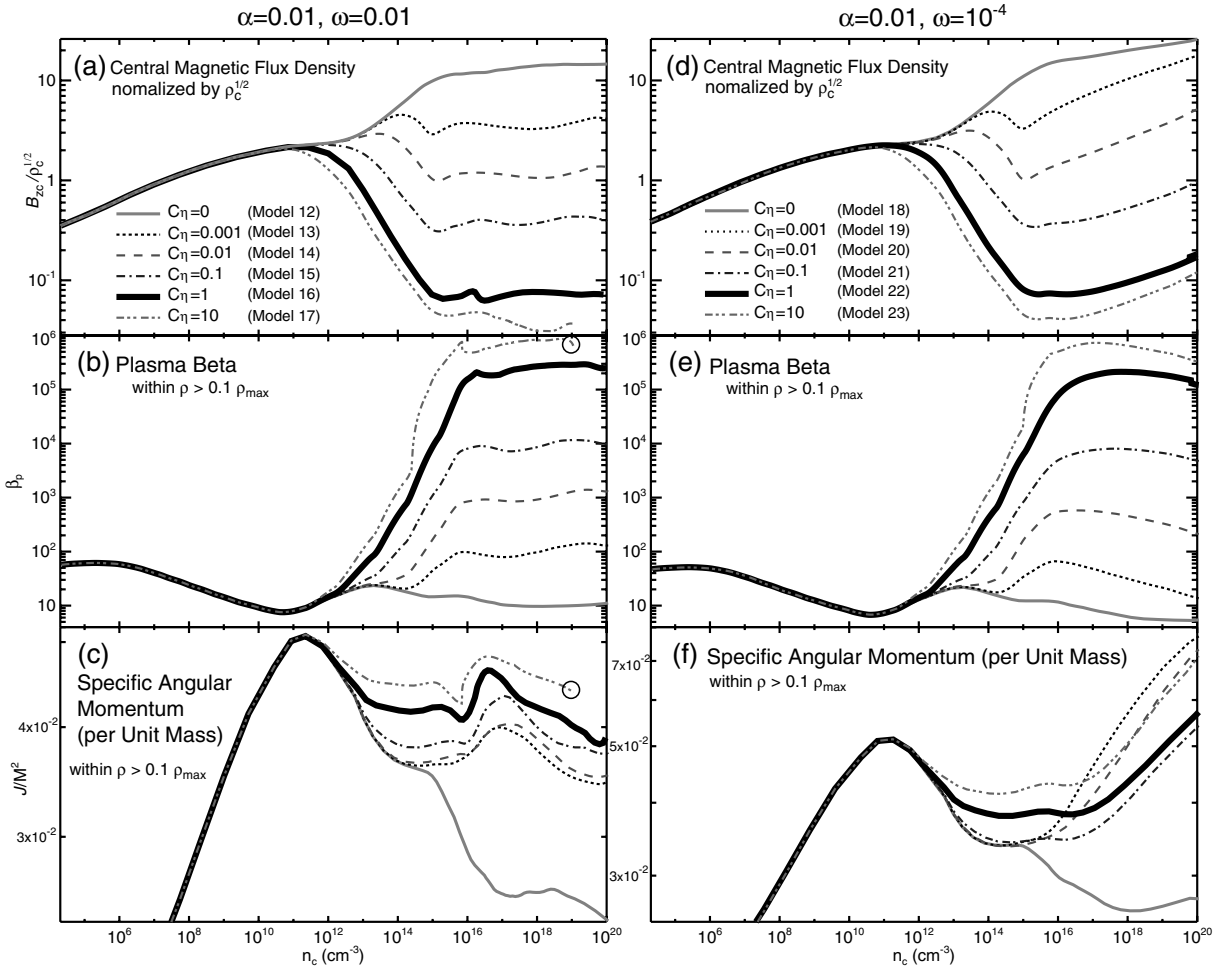

Fig. 6.— Evolution with different model of diffusivity η. Upper panels: Magnetic field ($B_{\rm zc}$) normalized by the square root of the density ($\rho_{\rm c}^{1/2}$) against the number density at the center of the cloud for Models 12-17 (left panel; *a*), and for Models 18-23 (right panel; *d*). Middle panels (*b* and *e*): Plasma beta within $\rho > 0.1\rho_{\rm c}$ for the same models as panels *a* and *d*. Lower panels (*c* and *f*): J/M^2 within $\rho > 0.1\rho_{\rm c}$ for the same models as panels *a* and *d*.

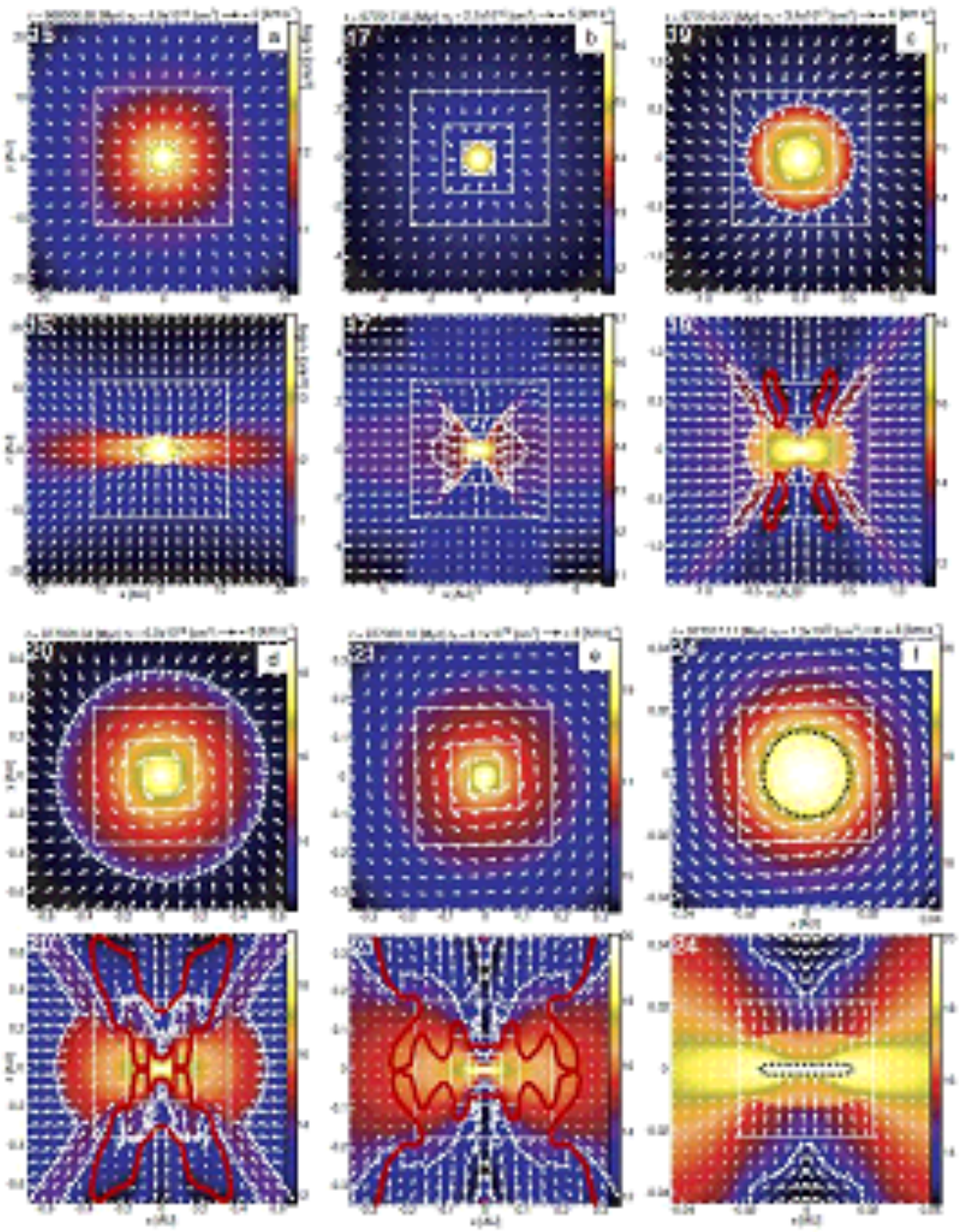

Fig. 7.— Same as Fig. 4 but for Model 16. Panels (a) through (f) are snapshots at the stages of (a) $n_c = 4.9\times10^{13}\,\mathrm{cm}^{-3}$ $(l = 15, 16)$, (b) $2.7\times10^{16}\,\mathrm{cm}^{-3}$ $(l = 17-20)$, (c) $3.4\times10^{17}\,\mathrm{cm}^{-3}$ $(l = 19-21)$, (d) $6.0\times10^{18}\,\mathrm{cm}^{-3}$ $(l = 20-23)$, (e) $8.1\times10^{19}\,\mathrm{cm}^{-3}(l = 21-25)$, and (f) $1.3\times10^{20}\,\mathrm{cm}^{-3}(l = 24, 25)$, where l denotes the level of subgrid. Dotted lines indicate the first core (white) and second core (black) which are surrounded by the shock surfaces. Red thick lines indicate the border between the infalling and outflowing gas ($v_{\rm out} \geq 0$ km s^{-1}). The level of the subgrid is shown in the upper left corner of each upper panel. The elapsed time (t), density at the center ($n_{\rm c}$), and arrow scale are denoted in each panel.

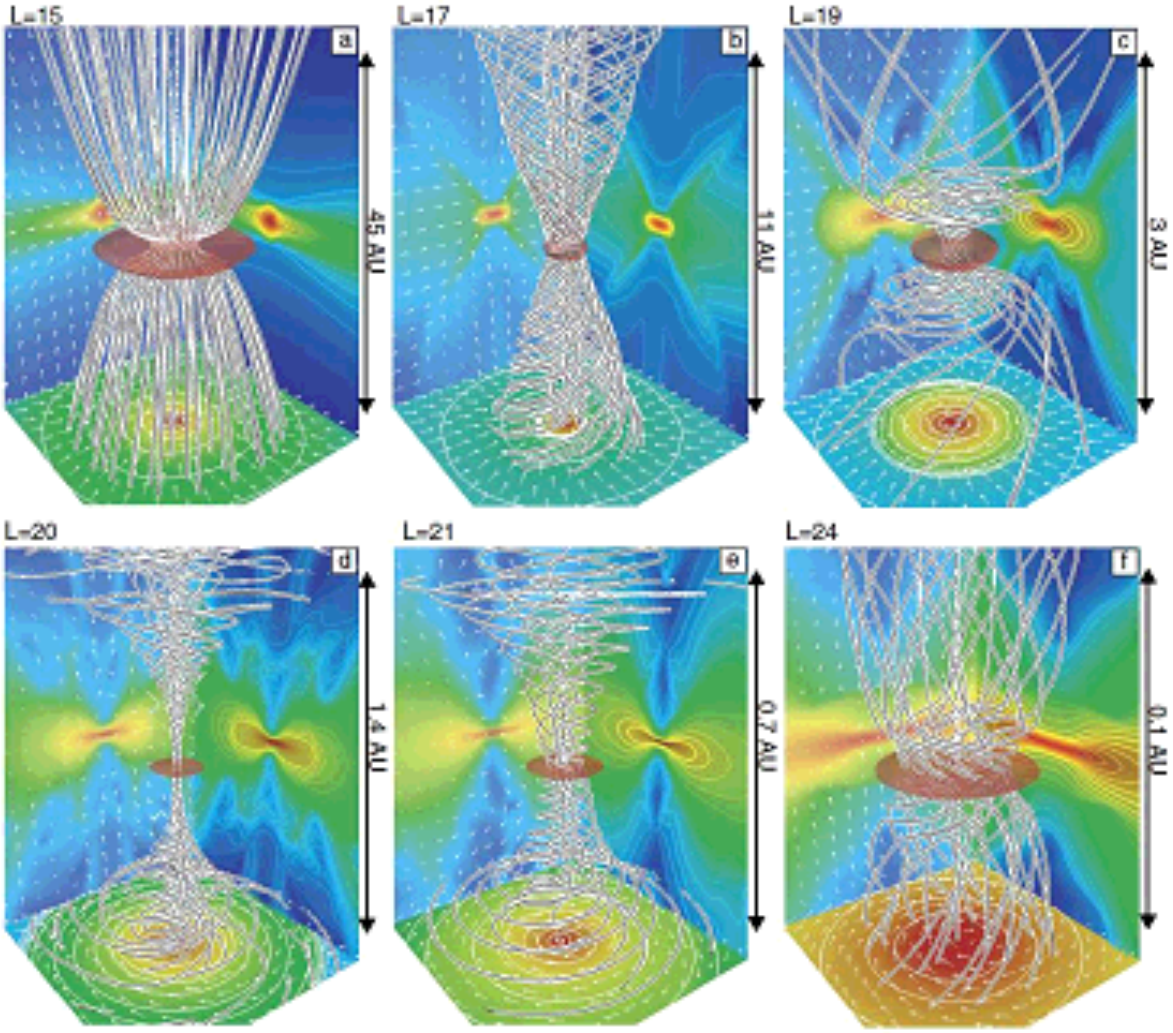

Fig. 8.— Same as Fig. 5 but for Model 16. Panels (a)-(f) are the same scale and same epoch as panels (a)-(f) of Fig. 7.

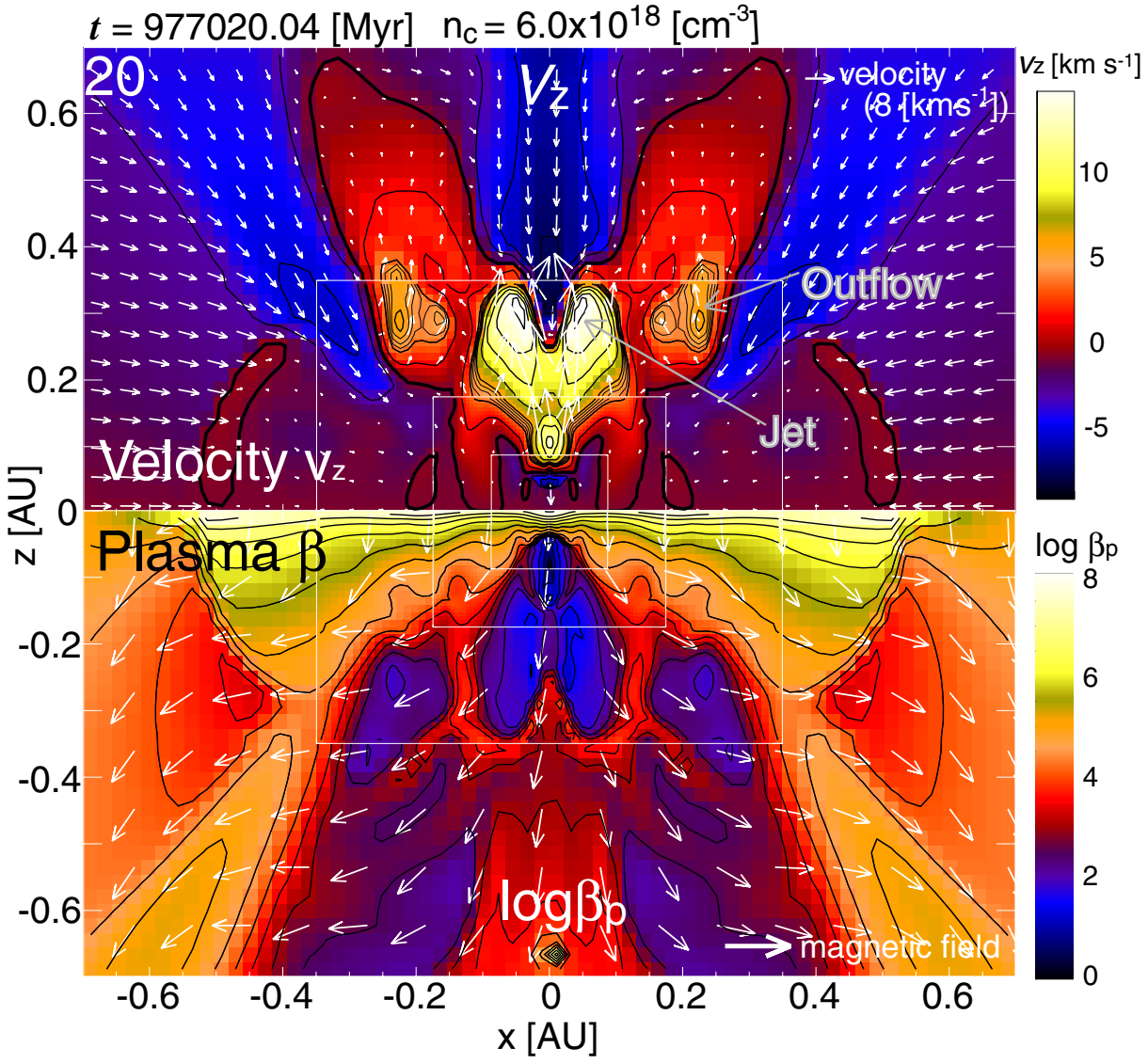

Fig. 9.— Velocity and plasma beta for Model 16 at the same scale and same epoch as Fig. 7*d*. Upper side ($z > 0$): Velocity of z-component (v_z; color-scale, contours) and velocity distribution (arrows) on the cross-section in the $y = 0$ plane. Lower side ($z < 0$): Plasma β ($\beta_{\rm p}$; color-scale, contours) and magnetic field (arrows) on the cross-section in the $y = 0$ plane.

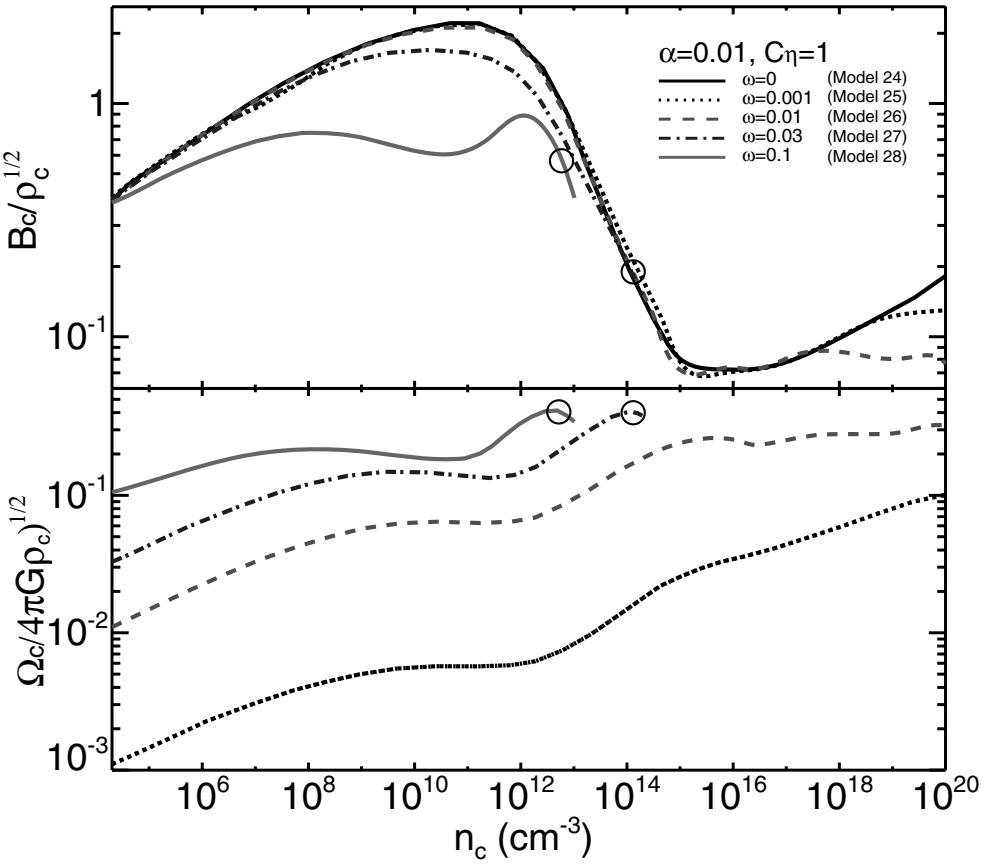

Fig. 10.— Evolutions of the magnetic field and angular velocity for various initial rotation rates. Upper panel: Magnetic field ($B_{\rm c}$) normalized by the square root of the density ($\rho_{\rm c}^{1/2}$) against the number density at the center of the cloud for Models 24-28. Lower panel: Angular velocity ($\Omega_{\rm c}$) normalized by the free-fall rate [$(4\pi G\rho_{\rm c})^{1/2}$] at the center of the cloud for Models 24-28.

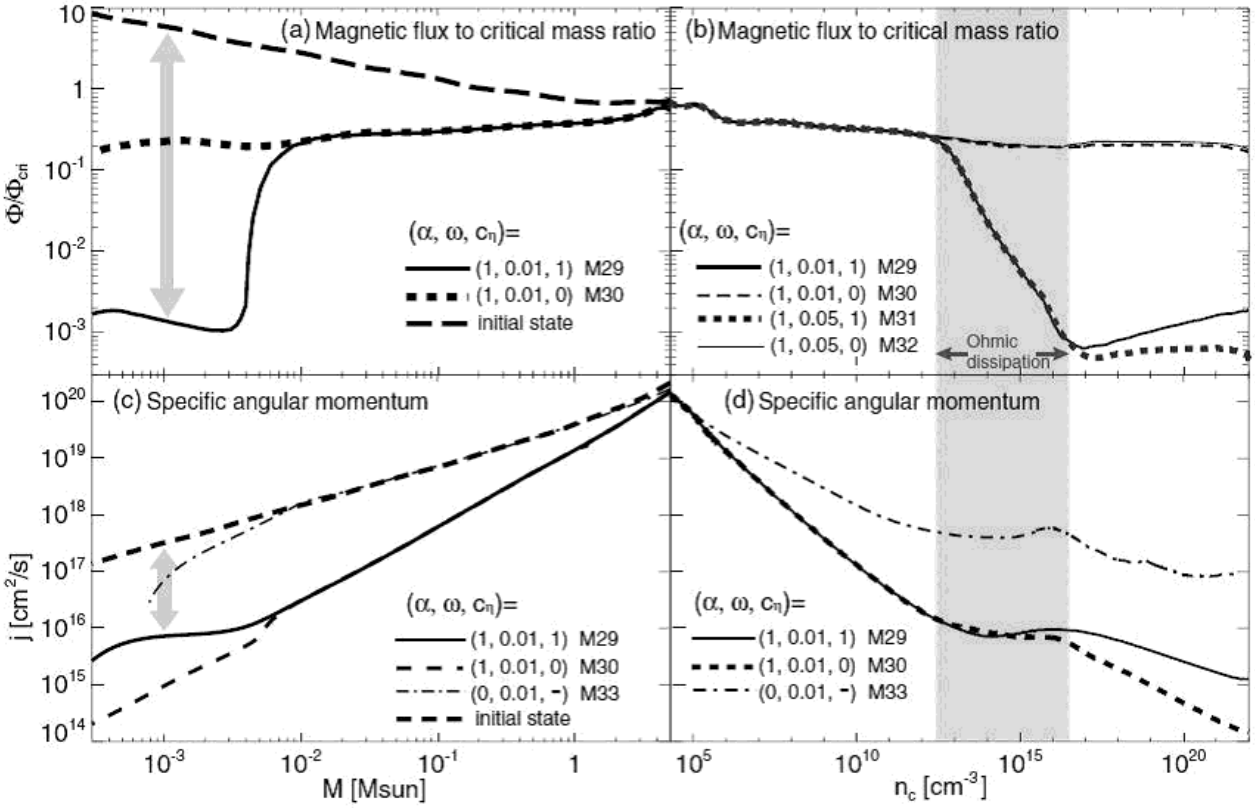

Fig. 11.— Panel (a): Spatial distribution of the magnetic flux. The magnetic flux normalized by the critical mass ($\Phi/\Phi_{\rm cri}$) as a function of the cumulative mass from the center of the cloud at the initial state (broken line), and at the end of the calculation for Models 29 (solid line) and 30 (dotted line) are plotted. Panel (b): Evolution of $\Phi/\Phi_{\rm cri}$ within $\rho > 0.1\rho_{\rm c}$ against the central number density for Models 29-32. Panel (c): Spatial distribution of specific angular momentum. Specific angular momentum (j) as a function of the cumulative mass from the center of the cloud at the initial state (thick broken line), and the end of the calculation for Models 29 (solid line), 30 (thin broken line), and 33 (dash-dotted line) are plotted. Panel (d): Evolution of j within $\rho > 0.1\rho_{\rm c}$ against the number density at the center of the cloud for Models 29, 30, and 33.